HHS Public Access

Author manuscript

Acta Biomater. Author manuscript; available in PMC 2018 February 01.

Published in final edited form as:

Acta Biomater. 2017 February ; 49: 507–520. doi:10.1016/j.actbio.2016.11.071.

Development of europium doped core-shell silica cobalt ferrite functionalized nanoparticles for magnetic resonance imaging

Bhavesh D. Kevadiya[1], **Aditya N. Bade**[1], **Christopher Woldstad**[2], **Benson J. Edagwa**[1], **JoEllyn M. McMillan**[1], **Balasrinivasa R. Sajja**[2], **Michael D. Boska**[2], and **Howard E. Gendelman**[1,*]

[1]Department of Pharmacology and Experimental Neuroscience, University of Nebraska Medical Center, Omaha, NE, United States, 68198-5880

[2]Department of Radiology, University of Nebraska Medical Center, Omaha, NE, United States, 68198-1045

Abstract

The size, shape and chemical composition of europium (Eu^{3+}) cobalt ferrite (CFEu) nanoparticles were optimized for use as a “multimodal imaging nanoprobe” for combined fluorescence and magnetic resonance bioimaging. Doping Eu^{3+} ions into a CF structure imparts unique bioimaging and magnetic properties to the nanostructure that can be used for real-time screening of targeted nanoformulations for tissue biodistribution assessment. The CFEu nanoparticles (size ~7.2 nm) were prepared by solvothermal techniques and encapsulated into poloxamer 407-coated mesoporous silica (Si-P407) to form superparamagnetic monodisperse Si-CFEu nanoparticles with a size of ~ 140 nm. Folic acid (FA) nanoparticle decoration (FA-Si-CFEu, size ~ 140 nm) facilitated monocyte-derived macrophage (MDM) targeting. FA-Si-CFEu MDM uptake and retention was higher than seen with Si-CFEu nanoparticles. The transverse relaxivity of both Si-CFEu and FA-Si-CFEu particles were r_2= 433.42 $mM^{-1}s^{-1}$ and r_2= 419.52 $mM^{-1}s^{-1}$ (in saline) and r_2= 736.57 $mM^{-1}s^{-1}$ and r_2= 814.41 $mM^{-1}s^{-1}$ (in MDM), respectively. The results were greater than a log order-of-magnitude than what was observed at replicate iron concentrations for ultrasmall superparamagnetic iron oxide (USPIO) particles (r_2= 31.15 $mM^{-1}s^{-1}$ in saline) and paralleled data sets obtained for T_2 magnetic resonance imaging. We now provide a developmental opportunity to employ these novel particles for theranostic drug distribution and efficacy evaluations.

Abstract

[*]**Corresponding author:** Howard E. Gendelman, M.D.; Department of Pharmacology and Experimental Neuroscience; University of Nebraska Medical Center; Omaha, NE 68198-5880; hegendel@unmc.edu; Tel.: (402) 559-8920; Fax: (402) 559- 559-3744.

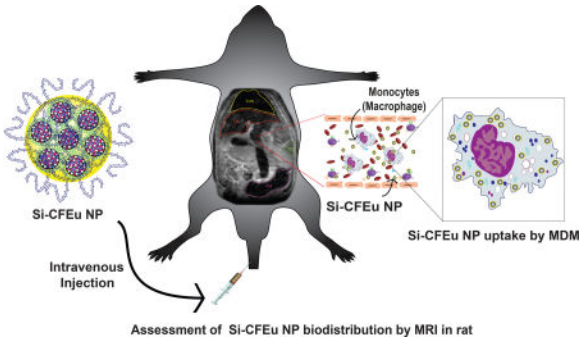

Keywords

Biodistribution; Cobalt ferrite; Multimodal imaging; Nanoprobes; Monocyte-Macrophages; Magnetic resonance imaging

1. Introduction

The use of monocyte-macrophage cell based nanoparticle drug carriage can improve the pharmacokinetic and pharmacodynamic profiles for treatment of human immunodeficiency virus (HIV), inflammatory and degenerative disorders [1–18]. A major obstacle for bench to bedside translation of the cell based nanoparticles rests in optimizing drug particle tissue biodistribution. This is especially true for research directives designed to improve treatment outcomes [19]. In the case of HIV/AIDS such approaches may one day lead to viral eradication by facilitating sustained release of antiretroviral drugs (ARVs) at viral reservoir tissue sites. Indeed, targeting drug nanoparticle delivery systems to macrophages encourages transport to sites of viral growth and inflammation as such sites harbor residual virus that cannot be eliminated by current ARV therapy. Elimination of resultant latent infections will require optimal delivery of therapeutic payloads designed to excise HIV from sites of host chromosomal integration [6, 11, 12, 20, 21]. As a first step towards achieving such goals we synthesized nanoparticles with combinations of ultra-small superparamagnetic iron oxide particles (USPIO) and ARV to speed assessment of drug tissue biodistribution [9, 21]. However, several limitations were seen with such an approach. *First*, while such small magnetite ART (SMART) particles reflected drug tissue distribution they failed to reflect complete drug biodistribution in viral reservoirs. *Second*, there were clear limitations seen for SMART sensitivity. *Third*, the specificity of SMART as tracking was not operative for all macrophage populations within the reticuloendothelial system. *Fourth*, while tracking of viral infection is absolutely mandatory for tracking of residual virus success can only be achieved in an infected host with improved particle imaging resolution and drug carrying capacities [22–26]. Reflective of these ends, successes were recently seen for targeted cancer drug delivery systems. These works employed T_2- or T_2*-weighted magnetic resonance imaging (MRI) theranostics [27–30].

Based on all prior experiences, we now posit that cobalt ferrite (CF) nanoparticles perhaps hold optimal physicochemical properties for theranostic ARV-bioimaging applications based on their abilities to sustain drug payloads and determine drug distribution as was

demonstrated for doxorubicin [30]. An added benefit of this system revolves around its magnetic feature that can affect proton relaxation with transverse relaxivity as well as its luminescence properties [30, 31]. The combination of fluorescence and magnetic properties, “dual-modality imaging” enables histological confirmation of drug loading, tissue pathology and ARV particle release [31, 32].

To such ends, in the current report, we investigated the role that CF particles may play in macrophage drug transport. In a first step towards such goals, europium (Eu^{3+}) doped CF (Si-CFEu) nanoparticles with highly crystalline unique dual-modality imaging properties (magnetic and fluorescence) were made and shown to be rapidly endocytosed by macrophages through nanoparticle decoration. The folate receptor (FR) present on the macrophage surface [33, 34] was engaged by placing folic acid (FA) on the particle surface. This enabled the synthesized particles to seek out the FR and potentially enhance drug delivery in cell culture as was previously demonstrated [6, 9, 20, 21, 35, 36]. These next generation FA decorated probes combine accurate histologic (fluorescent) and magnetic properties to facilitate the utility of multimodal nanoprobes. The MRI tests employed showed accurate assessments of nanoparticle biodistribution and histology. The sensitivity and specificity of the imaging system was enhanced over conventional USPIO particles. The formulations have drug carriage capacities and as such provide future potential usage in bringing ARVs to viral reservoirs. All together, we posit that targeted Si-CFEu multimodal imaging nanoprobes represent a unique platform for theranostic applications to diagnose disease and monitor therapeutic efficacy.

2. Materials and Methods

2.1. Chemicals

Iron(III) acetylacetonate (Fe(acac)3), cobalt (II) acetylacetonate (Co(acac)2), europium(III) nitrate hydrate (Eu(NO3)3•5H2O), tetraethyl orthosilicate (TEOS), 1,2-hexadecanediol, (3-mercaptopropyl) trimethoxysilane (MPTS), poloxamer 407 (P407), folic acid (FA), cetyltrimethylammonium bromide (CTAB), oleic acid, and oleylamine, lipopolysaccharide (LPS), 3-(4,5-dimethylthiazol-2-yl)-2,5-diphenyltetrazolium bromide (MTT), low gelling temperature agarose, iron and cobalt standards for ICPMS (TraceCERT®) and nitric acid (TraceSELECT®) were obtained from Sigma-Aldrich, St. Louis, Missouri, USA. Recombinant human macrophage-colony stimulating factor (MCSF) was obtained from Wyeth Institute., Cambridge, MA, USA. All other reagents and solvents were used without further purification. Millipore water (18.0 M Ω cm) was used for all experiments.

2.2. Human monocyte-derived macrophages (MDM)

Human peripheral blood monocytes were obtained by leukapheresis from hepatitis B and HIV-1/2 seronegative donors and were purified by counter-current centrifugal elutriation. Cells were cultured in Dulbecco's modified Eagle’s medium (DMEM; Invitrogen, Grand Island, NY, USA) with 10% heat-inactivated pooled human serum (Innovative Biologics, Herndon, MA, USA), 1000 U/ml macrophage colony stimulating factor (MCSF), 1% glutamine, 50-μg/ml gentamicin, and 10-μg/ml ciprofloxacin [37] for 7 days to promote differentiation into macrophages.

2.3. Animals

Male Sprague Dawley rats (160–170 g) were obtained from Charles River Laboratories, Wilmington, Massachusetts, USA. Animals were housed in the University of Nebraska Medical Center (UNMC) laboratory animal facility according to Association for Assessment and Accreditation of Laboratory Animal Care guidance. All protocols related to animal experiments were approved by the UNMC Institutional Animal Care and Use Committee, and met the requirements of the UNMC ethical guidelines set forth by the National Institutes of Health.

2.4. Synthesis of CFEu nanoparticles

A stepwise synthesis scheme of CFEu nanoparticles is outlined in Fig. 1. The process involved thermal decomposition of cobalt acetylacetonate, iron (III) acetylacetonate and europium (III) nitrate hydrate in the presence of oleic acid and oleylamine (Fig. 1A). Oleic acid and oleylamine were used as surfactants that served as attachment sites for particle targeting moieties. Benzyl alcohol served both as solvent and protective ligand, while 1,2-hexadecanediol was used as the reducing agent [38, 39]. Briefly, Fe $(acac)_3$ (706 mg, 2 mmol), $Co(acac)_2$ (257 mg, 1 mmol), $Eu(NO_3)3•5H_2O$ (100 mg, 0.29 mmol), 1,2-hexadecanediol (2.584 g, 10 mmol), 5 ml of oleic acid, 5 ml of oleylamine, and 30 ml of benzyl ether were mixed and sonicated for 2 min using a probe type sonicator (Cole-Parmer, Vernon Hills, IL, USA). The mixture was transferred into a Teflon-lined stainless steel autoclave reactor and allowed to react in a preheated vacuum oven at 260°C for 90 min then cooled to room temperature. Ethanol was added to precipitate the CFEu nanoparticles that were then collected using a magnetic separator. The crude particles were filtered, washed several times with absolute ethanol then vacuum dried at 60°C for 12 h. The synthesized crystalline CFEu nanoparticles exhibited hydrophobic properties upon resuspending in chloroform or hexane.

2.5. Synthesis of FA decorated CFEu nanoparticles encased in mesoporous Si-spheres

To facilitate screening and biodistribution of ligand modified FA-Si-CFEu nanoparticles with a poloxamers 407 coating were synthesized (Fig. 1B). The FA functionalized particles were produced using a premix of 450 mg of unmodified and 50 mg of FA modified poloxamer 407 (P407) [12]). Briefly, the poloxamers were dissolved in 180 mL of distilled water under light protection. In a separate beaker, CFEu nanoparticles were dispersed in 3 ml of chloroform and added to an aqueous solution containing CTAB (20 ml, 400mg). The CFEu and CTAB mixture was stirred vigorously until a homogeneous oil-in-water microemulsion was formed. This microemulsion was heated at 60 °C for 30 min to remove chloroform. After chloroform evaporation, the obtained aqueous phase containing micelles of CTAB-CFEu was syringe filtered (13 mm, 0.22 μm, Fisherbrand Syringe Filters, Fisher Scientific, Pittsburgh, PA, USA). The filtrate was then mixed with the poloxamer solution and reacted at 80°C for 1h. An aqueous solution of 2 M NaOH (1.4 mL) was then added to the reaction mixture after which a premix of freshly prepared 2 mL tetraethyl orthosilicate (TEOS) and 0.4 mL mercaptopropyl trimethoxysilane (MPTS) was added into the same flask. Stirring at 80°C was continued for 120 min after which the mixture was cooled to room temperature and filtered under vacuum. The resulting FA-Si-CFEu nanoparticle

suspension was purified by adding ethanol followed by stirring at 50°C for 16 h. The mixture was then centrifuged at 18,000 rpm, 10°C for 30 min (Sorvall, Lynx-4000 superspeed centrifuge, Thermo Fisher Scientific, Waltham, MA, USA) and reconstituted in ultrapure water, characterized and stored at 4°C for subsequent use. Non-targeted Si-CFEu nanoparticles were prepared in an analogous manner with exclusion of FA-P407 from the reaction mixture. The FA/Si-CFEu nanoparticles were monodisperse and characterized with narrow size distribution with long period stability (supplementary data; Fig.S1).

2.6. Ultrasmall superparamagnetic iron oxide particles (USPIO)

USPIO with size ~ 67.3 nm were fabricated in our laboratory using functional alendronate-coated iron oxide particles [21]. These were employed for comparative studies with the newly synthesized FA/Si-CFEu nanoparticles.

2.7. Characterizations

Powder X-ray diffraction (XRD) analyses were carried out in the 2θ range of 2– 70° using a PANalytical Empyrean diffractometer (PANalytical Inc.; Westborough, MA, USA) with Cu-Kα radiation (1.5418 Å) at 40 kV, 45 mA setting. A mask of 20 mm and divergence slit of 1/32° were used on the incident beam path. A thin layer of the nanoparticles powder sample was placed on a zero background silicon plate and the sample holder was continuously spun at the rate of 22.5 deg/s during the measurements. The solid state PIXcel3D detector (PANalytical Inc.; Westborough, MA, USA) was scanned at a rate of 0.053 deg/s during data collection. The PIXcel3D was equipped with a beam monochromator to improve signal to noise ratio. Magnetic characterization was carried out using a superconducting quantum interference device (SQUID) magnetometer (Quantum Design, MPMS-XL, Quantum Design International (QDI), San Diego, CA, USA) at 300K. High-resolution transmission electron microscopy (HR-TEM) using a FEI Tecnai Osiris microscope equipped with a Gatan Orius CCD camera (FEI, Houston, TX, USA) and selected area electron diffraction (SAED) was used to characterize the internal morphology and structure of nanoparticles. The microscope was equipped with a double-tilt stage and energy-dispersive detector (EDS) operated at 200 kV. The samples were prepared in toluene/Milli-Q water and dried on a copper grid (FCF-400-CU, Electron Microscopy Sciences–EMS, Hatfield, PA, USA) at room temperature and bright field images were taken with exposure times of 2s. No staining of nanoparticles was necessary since the contrast between CF and Si was adequate. The EDS data sets were collected on a ChemiSTEM system and analyzed with the Bruker Esprit software (Bruker, Billerica, MA, USA). The experimental SAED patterns were analyzed using PCED2 software (Landyne Software, Lincoln, NE, USA). Particle size measurements from TEM micrographs were analyzed using Image-J software (https://imagej.nih.gove/ij/). For TEM analysis thin sections (100 nm) of control and nanoparticle-loaded MDM were cut using a Leica UC6 ultramicrotome (Leica Microsystems Inc., Buffalo Grove, IL, USA) then placed on 200 mesh copper grids and examined using the Tecnai G2 Spirit TWIN electron microscope (FEI, Houston, TX, USA) operating at 80kV. Images were acquired with an AMT digital imaging system. Stability of the FA/Si-CFEu nanoparticle suspension was assessed at 4°C for 3 weeks by measuring hydrodynamic diameter and particle size distribution in saline on a Malvern Nano-Series Zetasizer system (Malvern Instruments Ltd., Malvern, UK). Atomic-force microscopic (AFM) analysis was performed on a Bruker

Dimension Icon® Atomic Force Microscope (Bruker, Billerica, MA, USA) equipped with peak-force Tapping and scan-Asyst with Al reflection coating (spring constant is 0.4 N/m and tip radius is about 2 nm, width 25 um, thickness 0.65 um, and length 115 um). Multilayers of nanoparticles were prepared by drop casting diluted aliquots of aqueous nanosuspensions on clean glass slides followed by slow evaporation of the solvent at room temperature. The images were flattened using Nano-Scope Analysis software (Bruker; Billerica, MA, USA). Fourier transform infrared spectra (FTIR) were recorded on a Perkin-Elmer-spectrum attenuated total reflectance (ATR)-FTIR equipped with a UATR-accessary (Perkin-Elmer Inc; Waltham, MA, USA). Thermogravimetric analysis was carried out in the temperature range of 30–800°C at a heating rate of 10°C/min under nitrogen flow of 20 ml/min (Simultaneous Thermal Analyzer (STA)-6000, Perkin-Elmer Inc.; Waltham, MA, USA). Iron and cobalt content were determined by inductively coupled plasma mass spectrometry (ICP-MS; ICP-MS-300Q; PerkinElmer Inc.; Waltham, MA, USA), using operating parameters of plasma flow = 16.0 l/min, auxiliary flow = 1.2 l/min and nebulizer gas flow = 0.95 l/min.

2.8. In vitro relaxometric measurements-phantom study

Suspensions of FA/Si-CFEu and USPIO in the concentration range of 0.035 – 0.35 mM iron were prepared in Dulbecco's phosphate-buffered saline (DPBS; Thermo Fisher Scientific, Waltham, MA, USA). A 1.5 % (w/v) agar gel was prepared by adding 150 mg of low melting agar in 10 mL of PBS at 70°C for 30 min. For preparing phantom gels containing nanoparticles, 100 μL of the 1.5% (w/v) agar solution, preheated to 60 °C to prevent gelation, was mixed with 100 μL of FA/Si-CFEu and USPIO nanoparticle suspensions. These experiments were performed in triplicate for each employed concentration. The FA/Si-CFEu and USPIO nanoparticle suspensions and agar gels were vortexed thoroughly while warm in 250 μL eppendorf tubes, ensuring no air bubbles were present, and then rapidly cooled in an ice bath. The eppendorf tubes containing the fixed FA/Si-CFEu and USPIO nanoparticles in agar gels were suitable for MRI tests. T_2-relaxtivity was measured using (7T/16cm Bruker PhamaScan, Bruker; Ettlingen, Germany). Relaxivity images were generated using a CPMG (Carr Purcell Meiboom Gill sequence) phase cycled single slice, multi echo sequence. A single slice (0.5 mm slice thickness) image was acquired with an acquisition matrix of 256 × 128 mm, 50 mm field of view, 50 echoes at 10 ms echo time, 10 ms echo spacing, repetition time of 3000 ms, 2 averages, for a total acquisition time of 13 minutes.

To measure the T_2-relaxivity in MDM, cells were seeded onto 100 mm culture plates at a concentration of 10^6 cells/ml. After seven days of cultivation media was changed to that containing 150 ng/ml FA/Si-CFEu particles. After 8 h the treatment medium was removed and cells washed three times with DPBS. Cells were then collected by centrifuge (3000 rpm for 8 min at 4°C) and suspended at various cell concentrations in DPBS containing 1.5% (w/v) agar solution in 250 uL eppendorf tubes. T_2-relaxtivity were acquired using MRI/MRS scanner (Bruker., Ettlingen, Germany). A CPMG phase cycled 3-dimensional multi-echo sequence was used for relaxivity imaging in cells. Images were acquired with an acquisition matrix of 128 × 128 × 64, 70 × 64.76 × 42.38 mm field of view, 48 echoes at 2.618 ms first

echo time and 2.618 ms echo spacing, repetition time of 250 ms, one average, for a total acquisition time of 34 minutes.

2.9. Real-time Si-CFEu and USPIO nanoparticle biodistribution by MRI

Real-time biodistribution of Si-CFEu or USPIO nanoparticles was determined in male Sprague Dawley rats. The animals were arbitrarily distributed into two groups each containing five animals. The first group received USPIO nanoparticles and the second group received Si-CFEu nanoparticles. Twenty-four hours prior to nanoparticle treatment rats were given 5 mg/kg lipopolysaccharide (LPS; Sigma-Aldrich, St. Louis, MO, USA) by intraperitoneal injection to generate a systemic inflammatory response and activate macrophages. Rats were given an MRI scan immediately prior to intravenous injection of Si-CFEu or USPIO nanoparticles (1 mg iron/kg iron content is injected for all cases) and 24 hours post-injection. Animals given Si-CFEu nanoparticles were also scanned at day 5-post injection to determine their temporal efficiency. MRI was acquired using a 7T/16cm Bruker PharmaScan MRI/MRS scanner (Bruker., Ettlingen, Germany). Biodistribution of Si-CFEu or USPIO nanoparticles was determined by MRI using T_2 mapping and T_2* weighted high-resolution imaging. A CPMG phase cycled 3-dimensional multi-echo sequence was used for T_2 mapping. Images were acquired with an acquisition matrix of 128 × 128 × 64, 70 × 64.76 × 42.38 mm field of view, 48 echoes at 2.618 ms first echo time and 2.618 ms echo spacing, repetition time of 250 ms, one averages, for a total acquisition time of 34 minutes. T_2* weighted MRI were acquired using a 3D spoiled gradient recalled echo sequence with echo time = 2.7 ms, repetition time = 2.7 ms, 15 degree pulse angle, 75 × 57.5 × 37.5 mm field of view (FOV), 256 × 196 × 128 acquisition matrix, six averages, for a total scan time of 25 minutes.

T_2 maps were reconstructed using custom programs written in Interactive Data Language (IDL; Exelis Visual Information Solutions; McLean, VA, USA). Pre-injection and 24 hour post-injection maps of Si-CFEu and USPIO nanoparticles were constructed using the even-echo images from the CPMG phase cycled imaging data set. Mean tissue T_2 was determined using region of interest (ROI) analyses before and after Si-CFEu or USPIO nanoparticles injection for the 24-hour results. The concentrations of Si-CFEu or USPIO nanoparticles were determined from the change in relaxivity ($\Delta R_2 = 1/T_{2\text{preinjection}} - 1/T_{2\text{postinjection}}$) and the per milligram nanoparticles relaxivity (r_2) determined as the slope of iron concentration versus R_2 measured *ex vivo*. The ROI analysis was performed using Image-J (http://imagej.nih.gov/lj) software.

2.10. Immunocytochemistry

To determine cellular distribution of Si-CFEu nanoparticles in different tissues, after the second MRI scan (five days after administration of Si-CFEu nanoparticles) rats were euthanized, and tissues were collected. Tissues were fixed in 4% paraformaldehyde (PFA) overnight and embedded in paraffin. Five μm thick tissue sections were cut and mounted on glass slides. Tissue sections were probed with rabbit anti-rat polyclonal antibody to ionized calcium binding adaptor molecule-1 (Iba-1) (1:500; Wako Chemicals, Richmond, VA, USA) to detect macrophages. Primary antibody was detected with anti-rabbit secondary antibody conjugated to Alexa Fluor 594. Nuclei were labeled with DAPI (4,6-diamidino-2-

phenylindole). Slides were cover-slipped with ProLong Gold anti-fade reagent (Invitrogen, Carlsbad, CA, USA). Slides were stored at −20°C. Images were captured with a LSM 810 microscope using a 63× oil lens (Carl Zeiss Microimaging, Inc., Thornwood, NY, USA).

2.11. Toxicology

Toxicity of the Si-CFEu nanoparticles was determined by serum chemistry and histological examination. For histological examination, 5 μm sections of paraffin-embedded tissues (liver, spleen, and lung) were affixed to glass slides and stained with hematoxylin and eosin. Images were captured with a 20× objective using a Nuance EX multispectral imaging system affixed to a Nikon Eclipse E800 microscope (Nikon Instruments, Melville, NY, USA). Histopathological assessment was conducted in accordance with the guidelines of the Society of Toxicologic Pathology.

For serum chemistry analysis, rat blood samples were collected before and five days after Si-CFEu administration. Albumin (ALB), alanine aminotransferase (ALT), total bilirubin (TBIL), phosphate (PHOS), total protein (TP) and amylase (AMY) were quantitated using a VetScan comprehensive diagnostic profile disc and a VetScan VS-2 instrument (Abaxis Veterinary Diagnostics, Union City, CA, USA).

3. Results

3.1. Structural and physicochemical properties of nanoparticles

3.1.1. Structural properties of the synthesized CF, CFEu and FA/Si-CFEu nanoparticles—Fig. 2A shows the X-ray powder diffraction (XRD) patterns of the CF, CFEu, and FA/Si-CFEu nanoparticles. All the diffraction peaks observed corresponded to the spinel ferrite structure. Phase identifications were carried out with matching experimental diffractograms to a standard ICDD PDF-4+ database (card number:04–016–3954 and 00–065–0586). TEM and XRD analyses confirmed the core-shell of the FA/Si-CFEu nanoparticles, characterized by a peak with 2θ at 22.4°-23.3° indicating uniform mesoporous Si coverage. Six characteristic XRD peaks indexed at 30.2, 35.5, 43.2, 53.6, 56.9 and 63.0° correspond to (220), (222), (331) and (400) crystal planes. The XRD peaks changed from (511), (440) and (311) to (422), (333) and (222) planes after incorporation of Eu^{3+}. The change in the crystal plane was linked to rearrangements in the CFEu crystal lattice. The ionic radius of Eu^{3+} is bigger than that of Co^{2+} and Fe^{3+} and therefore prefers to occupy the octahedral-B sites causing Co^{2+} to move from octahedral to tetrahedral-A sites of the spinel lattice [40, 41]. The inverse spinel structure of CF has previously been observed, where Co^{2+} ions have been shown to be octahedrally coordinated while Fe^{3+} complexes can be either tetrahedral or octahedral complexes [41, 42]. The crystal plane change was confirmed by simulated data sets of selected area electron diffraction (SAED) patterns. The average particle size was calculated using the Debye-Scherrer equation, $D = K\lambda/\beta\cos\theta$, where, θ is the Bragg diffraction angle, K is Plank's constant, λ is the wavelength source (1.541 Å), and β is the width of the XRD peak at half maximum height (0.9° at $2\theta = 35.7°$). The calculated average particle size of the CFEu was ~ 9.7 nm. The XRD data sets mirrored what was reported previously on CF nanoparticles [40, 41, 43–46].

3.1.2. Magnetic properties CF, CFEu and FA/Si-CFEu nanoparticles—We evaluated the magnetic properties of the synthesized CF, CFEu and FA/Si-CFEu nanoparticles using superconducting quantum interference device (SQUID). Fig. 2B shows that the saturation magnetization measurements for CF, CFEu, Si-CFEu and FA-Si-CFEu were 67.15, 47.05, 5.15 and 5.3 emu/g, respectively. This demonstrates that both particle size and Eu^{3+} cation inclusion results in dramatic changes in magnetic particle properties. Magnetic particles below a size threshold of 30 nm are known to be strongly attracted to magnetic fields but lose this feature after withdrawal of an external force. The results demonstrated that saturation magnetization decreased after doping Eu^{+} ions in CF nanoparticles. This can be due to the presence of paramagnetic ions at 300K and structural rearrangements in the original octahedral and tetrahedral sites upon Eu^{3+} insertion. The characteristic arrangements of the cations in the octahedral and tetrahedral spinel sites in the CF structure may be significantly affected by the Eu^{3+} doping [40, 47]. Additionally, doping of Eu^{3+} ions may disrupt the regular symmetry by moving the Co^{2+} ions from the octahedral to tetrahedral sites. This is a specific move of Co^{2+} ions as compared to the Fe^{3+} ions, since the Co^{2+} ions have larger ionic radii than Fe^{3+} ions. The magnetic properties of spinel ferromagnetic materials depend on the negative Fe^{3+}-Fe^{3+} interactions through spin coupling of $3d^5$ electrons [41]. At 300K, the Fe^{3+}-Fe^{3+} interactions decreased and Fe^{3+} ions exchanged with highly paramagnetic Eu^{3+} ions. The highly localized 4f electrons that contribute to the magnetic properties of Eu^{3+} cause weak 4f–3d interaction between Eu^{3+}–Fe^{3+} and indirect 4f–5d–4f electron coupling between Eu^{3+}–Eu^{3+} ions [40]. Therefore the overall number of Co^{2+} ions in the octahedral sites is reduced, which affects the magnetic properties of the CFEu by dropping anisotropy of the Co^{2+} ions present in the crystal lattice and thereby reducing the saturation magnetization value. The low coercivity and saturation magnetization parameters of the FA/Si-CFEu nanoparticles was posited due to the additional layer of Si-shell on CFEu nanocrystals (Fig. 2B inset; blue and green line).

3.1.3. High-resolution transmission electron microscopy (HR-TEM)—HR-TEM images of CFEu and Si-CFEu nanoparticles are shown in Fig. 3 and demonstrate that the CFEu nanoparticles consist of monodispersed nanocrystals with uniform particle sizes of ~7.2 nm (Fig. 3A and B). The CFEu particles consisted of faceted-hexagonal shaped monodisperse nanodiamonds bearing sharp edges (Fig. 3C). These particle physicochemical characteristics are consistent with CF nanoparticles produced by other methods, suggesting that the solvothermal process used did not cause morphological changes to the nanoparticles [48–50]. To further characterize the synthesized magnetite particles, HR-TEM and SAED diffraction analysis was performed. As shown in Fig. 3D, distinct lattice fringe spacing at ~ 0.22 nm (~2.2 Å) corresponding to the *d* spacing of the (331) lattice planes of CFEu particles demonstrates the crystalline nature of the particles. SAED patterns correlated with individual atomic crystal planes for the spinel CF structure (Fig. 3E, PCED2.0, Landyne Software, Lincoln, NE, USA. Both simulated SAED and XRD patterns matched, further confirming the highly crystalline nature of Eu^{3+} doped CF nanoparticles. TEM of Si-CFEu nanospheres (Fig. 3F) demonstrates that they are composed of dark CFEu cores surrounded by light grey Si-P407 shells. Hydrodynamic size distribution measurements of USPIO, Si-CFEu and FA-Si-CFEu nanoparticles revealed particle sizes of ~70 nm, ~140 nm and ~140 nm, respectively with no aggregation (Fig. 3G). The presence of Co; Fe and Eu was

confirmed by elemental analysis by energy-dispersive X-ray spectroscopy (Fig. 3H). Atomic force microscopy (AFM) was used to characterize surface topography of the synthesized CFEu and FA/Si-CFEu nanoparticles. As shown in Fig. 4, the Si covering on CFEu did not cause noticeable morphological changes in the particles. Both CFEu and Si-CFEu nanoparticles appeared spherical with smooth and uniform surfaces (Fig. 4A and C). The three-dimensional arrangement of the spherical nanoparticles and diameter are shown in Fig. 4B and D.

3.1.4. Spectroscopy and thermal analysis—The absorption bands at 500–800 cm^{-1} in the FTIR spectra of CFEu nanoparticles are characteristic of stretching vibrations of octahedral metal-oxygen (M–O) bonds in the ferrite lattice (Fig. 5A). The asymmetric and symmetric stretching vibration bands linked to the Si-O-Si network in pristine Si (control silica) and Si-CFEu nanoparticles were observed at 1052 cm^{-1} and 800 cm^{-1}, respectively. The spectra of pristine P407 (control polymer) exhibited C-H and C-O stretching vibrations bands at 2887 cm^{-1} and 1100 cm^{-1}, fcell retention studies, MDM respectively (data not shown). The FTIR data is comparable to previously reported spectra for P407 coated Si nanoparticles [51, 52]. The spectrum of the FA-P407 displayed intense peaks at 1608 $cm^{-1}$and 1465 cm^{-1}, corresponding to the aromatic ring stretch of the pteridine ring and p-amino benzoic acid moieties of FA. Aromatic C-H stretching bands at 1056, 962, and 845 cm^{-1} further confirmed covalent linkage of FA onto P407. Significant peak broadening at 1620 cm^{-1} is attributed to the amide linkage between the polymer's polyoxyethylene amine and FA. These FT-IR results support successful coating of Si-CFEu nanoparticles with FA-modified P407. The thermogravimetric analysis curves (TGA) of CFEu and FA/Si-CFEu nanoparticles are shown in Fig. 5B. The steady weight loss of CFEu and FA/Si-CFEu from 40 to 120°C is attributed to elimination of free water. The CFEu nanoparticles lost about 20–25% weight in the range of 200–400°C due to removal of structural water. The minor weight loss between 550°C and 650°C could be attributed to structural changes in CFEu nanoparticles in the second stage. Si-CFEu and FA-Si-CFEu nanoparticles lost ~15–20 % and ~20–25 % weight at the temperature of the second phase, respectively. The observed trend in weight loss may indicate that the Si-P407-shell and FA-P407 serves to protect FA/Si-CFEu nanoparticles from degradation. The percent weight of Si in the FA/Si-CFEu nanoparticles is ~19–24%.

3.2. Uptake, retention and detection of intracellular FA/Si-CFEu in MDM

To determine cell uptake of the nanoparticles, MDM were treated with Si-CFEu and FA-Si-CFEu nanoparticles (based on 150 ng/mL iron) upto 8 h. Cells were washed with PBS and collected into nitric acid (69.0%) at different time points, 1 h, 2 h, 4h, and 8 h. Cobalt concentration was determined by ICP-MS. For cell retention studies, MDM were treated with Si-CFEu and FA-Si-CFEu nanoparticles (150 ng/mL iron) for 8 h; cells were washed with PBS and fresh medium was added. Half of the medium was changed every other day. MDM were collected on days 1, 5, and 10, and cobalt content was determined by ICP-MS. Statistical differences in cobalt content between Si-CFEu and FA-Si-CFEu treated groups were determined by Student's t-test at $p<0.05$. The FA-Si-CFEu nanoparticles were taken up significantly more by MDM than Si-CFEu nanoparticles (0.08 ± 0.009 and 0.05 ± 0.002 ng cobalt/10^6 cells, respectively, Fig. 6A). A greater number of particles (0.05 ±0.008 ng

cobalt/10^6 cells) were retained in the cells over 10 days with FA-Si-CFEu nanoparticles than with non-targeted Si-CFEu nanoparticles (0.02 ± 0.006 ng cobalt/10^6 cells), reflecting the initial higher cell uptake (Fig. 6B).

The presence of FA/Si-CFEu nanoparticles in MDM was determined by confocal microscopy using the natural fluorescence of europium and by transmission electron microscopy of CFEu particles (detailed methodology is described in supporting information, Fig.S4). MDM were treated with FA/Si-CFEu at 150 ng/mL iron for 8 h. For confocal microscopy experiments, MDM were washed with PBS after 8 hr treatment, and fixed with 4% PFA. Particles were detected using an excitation of 488 nm and emission of 510/520 nm. Images were captured with an LSM 810 microscope using a 63× oil lens. The intracellular localization of Si-CFEu nanoparticles as detected by europium fluorescence is illustrated in Fig. 6C. TEM illustrated that, as usual, FA/Si-CFEu nanoparticles were internalized into macrophage vesicular compartments (Fig. 6D–F). TEM of control MDM shows typical macrophage morphology (Fig. 6D). The presence of Si-CFEu and FA/Si-CFEu nanoparticles in MDM is shown in Fig. 6E and F. Higher magnification (zoom of red encircled areas (Fig. 6E (ii-iii) and F (ii-iii)) clearly shows the presence of nanoparticles visualized as black punctate structures within membrane-bound endosomes, with a higher number of nanoparticles internalized with FA-Si-CFEu compared to Si-CFEu treatment.

3.3. MRI relaxivity

To determine the MRI signal enhancement effects of FA/Si-CFEu compared to USPIO nanoparticles, the r_2 ($mM^{-1}s^{-1}$) of FA/Si-CFEu and USPIO nanoparticles in PBS as well as in MDM at different iron concentrations were determined using a 7T MRI scanner. The iron concentration in mM was plotted against R_2 (s^{-1}). The relaxivity of FA/Si-CFEu nanoparticles in MDM and in PBS varied linearly with the iron concentration as shown in Fig. 7. The corresponding signal intensities of T_2-weighted phantom images of Si-CFEu nanoparticles decreased, confirming the sensitivity of the FA/Si-CFEu nanoparticles (Fig. 7A). The concentration dependent relaxivity in PBS of Si-CFEu and FA-Si-CFEu nanoparticles was found to be r_2=433.42 mM^{-1} s^{-1}, and r_2=419.52 mM^{-1} s^{-1}, respectively (Fig. 7B), which are more than one log greater r_2 compared to our previous USPIO nanoparticles (r_2= 31.15 s^{-1} mM^{-1}Fe) [21]. Relaxivity measures of FA/Si-CFEu in MDM was linear with increased cellular iron concentrations (Fig. 7C). The relaxivity of Si-CFEu and FA-Si-CFEu nanoparticle-loaded MDM was found to be r_2=736.57 mM^{-1} s^{-1}, and r_2=814.41 mM^{-1} s^{-1}, respectively. These values were up to two fold greater than that observed in saline. This difference may be due to uniform distribution of nanoparticles in MDM and is consistent with a cellular bulk magnetic susceptibility relaxation mechanism based on static dephasing regime theory [53].

3.4. MRI imaging and biodistribution by relationship with immunohistology

The experimental timeline for the MRI scans in rats is depicted in Fig. 8A. Representative pre- and post-injection MR images of rats for USPIO (Fig. 8B) and Si-CFEu (Fig. 8C) are shown. Post-injection MR images were acquired 24 h after nanoparticle administration for both groups. In MR images, liver and spleen are identified (liver = red, spleen = green). The presence of USPIO and Si-CFEu nanoparticles within the rat produced a decrease in T_2,

subsequently resulting in a decrease of signal (post-USPIO and post-Si-CFEu (Fig. 8B, and C). The liver and spleen regions of the pre-injection images (Fig. 8B and C) are light gray in color. However, post-injection images of the liver and spleen regions (Fig. 8B and C) are significantly darker. There is substantially more signal loss in post-injection images of the Si-CFEu animals (Fig. 8C) compared to the signal loss in post-injection images of the USPIO treated group (Fig. 8B), despite a lower concentration of iron from the Si-CFEu particles (Fig. 9A). Liver and spleen iron concentrations were quantified by MRI and compared between Si-CFEu and USPIO nanoparticle-treated groups. Higher iron levels were observed in USPIO treated animals compared to Si-CFEu nanoparticles treated animals. The five-day MRI quantitation results were identical to the 24-hour results (data not shown). Fluorescence images of representative areas from the T_2 map-MRI (Fig.8 C, yellow boxed areas) for animals in the Si-CFEu group is presented in Fig. 9B.

3.5. Confocal microscopy and immunohistology

To determine cellular distribution of Si-CFEu nanoparticles in different tissues, paraffin embedded sections were evaluated by confocal microscopy for europium fluorescence properties and probed with Iba-1 antibody for detection of activated macrophages. Si-CFEu nanoparticles were readily detected in liver and spleen (Fig. 9B). Localization of the particles within tissue macrophages (Iba-1 red fluorescence) is shown in Fig. 10 (indicated by arrows in merged image) (Fig.10).

3.6.Toxicologic evaluation

To determine whether Si-CFEu nanoparticles induced systemic toxicity, blood and tissues were collected after the second MRI scan and following Si-CFEu injections. Blood samples were also collected 24 hours after LPS administration and prior to the Si-CFEu injections. No significant differences between pre- and post-treatment samples were observed for any hematologic or metabolic parameters (Fig. 11A) indicating that Si-CFEu particles did not adversely affect blood, liver, kidney or pancreatic functions. Histological examination of liver, spleen, and lung revealed no abnormal pathology following nanoparticle administration (Fig. 11B).

4. Discussion

Despite significant improvements in ART regimens a major obstacle to the development of long acting treatment for HIV/AIDS rests in assessment of drug tissue biodistribution and depots. To this end we reasoned that an immediate need exists to develop SMART nanoparticle platforms to improve diagnostic and therapeutic assessments for nanoART [9, 21]. While SMART approaches do reflect drug tissue distribution they have so far failed in their ultimate goal of reflecting drug particle distributions to viral reservoirs such as lymph nodes, gut and brain. The successful development of FA/Si-CFEu particles holds considerable promise to meet this challenge and the realization of a clinically useful theranostic screen.

FA/Si-CFEu nanoparticles could cargo diverse payloads and enter body areas where latent or restricted HIV-1 infection resides. Detection of virus in such body tissues remains a major

challenge in viral eradication [11, 22, 24, 25, 54, 55]. HIV-1 infection is continuous at low levels in lymphoid, gut and central nervous system compartments but exists as a source to propagate progeny infection [11, 22, 24, 25]. Thus, innovations that improve penetrance of ARV into HIV sanctuaries have remained a major focus in HIV cure strategies [25, 55].

CF nanomaterials have gained considerable interest in biomedical applications due to their unique properties [38, 56–62]. The spinel structure of CF allows for introduction of rare earth elements into the lattice (Nd:neodymium, Eu:europium, and Gd:gadolinium) to improve the magnetic properties of doped nanoparticles [40] and make them suitable as multimodal imaging nanoprobes for rapid screening of therapeutic agents and targeting ligands. The use of CF in clinical settings is limited by particle aggregation and their limited biocompatibility [58, 63]. Nonetheless, CFEu nanoparticles surface-modified with mesoporous Si that exhibit properties of biocompatibility and hydrophilicity is of immediate need in clinical practice.

To generate highly monodispersed FA/Si-CFEu nanoparticles, a co-condensation approach was used to functionalize the Si-P407 on CFEu nanocrystals. The formed FA/Si-CFEu nanoparticles exhibited exceptionally high r_2 proton relaxivity and superparamagnetism, fluorescent properties, and narrow size distribution. Importantly, mesoporous Si is chemically inert and has therefore found widespread use for functionalization of inorganic nanomaterials [64–68]. Moreover, mesoporous Si provides a hydrophilic stable matrix on the surface of the particles, which allows for surface engineering for targeting ligands and stabilizing surfactants [66, 68, 69].

Compared to conventional synthesis of magnetic nanoparticles by thermal decomposition and co-precipitation–based fabrication methods, the solvothermal technique offer a novel approach towards generating readily scalable CFEu nanoparticles with improved chemical yield. The Si-P407 coated CFEu nanoparticles were further functionalized with FA ligand for targeting macrophages. Physical and chemical properties characterized by means of XRD, SQUID, HR-TEM, AFM, FTIR and TGA-DTA confirmed the synthesis of CFEu and FA/Si-CFEu nanoparticles.

FA-Si-CFEu nanoparticles were taken up and retained more readily by MDM compared to non-targeted Si-CFEu. Macrophage internalization of FA-Si-CFEu and Si-CFEu nanoparticles can occur by receptor-mediated or endocytic mechanisms [12]. These results indicate that FA-Si-CFEu and Si-CFEu could enable the screening of ARV tissue biodistribution over extended time periods.

The T_2 relaxivity measurements confirmed the feasibility and sensitivity of FA/Si-CFEu and USPIO nanoparticles as T_2-contrast agents for rapid screening of ARV drug nanoparticles. Recently, Joshi et al. shown cobalt ferrite nanoparticles r_2 relaxivity of 110 to 345 mM^{-1} s^{-1} based on sizes of nanoparticles [56]. Our data showed that the T_2 relaxivities of FA/Si-CFEu nanoparticles are higher compared to USPIO as well reported in literature and the improved contrast indicates that the FA/Si-CFEu nanoparticles are more sensitive as multimodal imaging nanoprobes. This may be attributed to solid structural and magnetic properties of FA/Si-CFEu particles. Importantly, the higher relaxivity resulted in enhanced sensitivity for

determination of iron concentration, which will enable the detection of lower iron concentrations and improve the accuracy of determining differences in concentrations due to targeting moieties. To investigate the translational potential of the FA/Si-CFEu nanoparticles, rats were injected with LPS to generate a systemic inflammatory response. Following LPS injection, animals were given an IV bolus dose of 1 mg iron/kg of Si-CFEu nanoparticles. MRI of the animals showed decreased T_2 values and a corresponding signal decrease in reticuloendothelial tissues (liver and spleen). Si-CFEu nanoparticles were more sensitive and specific in MRI tests than USPIO nanoparticles used at the same dose. While the MRI signal in liver and spleen of rats treated with Si-CFEu nanoparticles was more intense compared to the same tissues of rats treated with USPIO, less iron was detected in Si-CFEu treated animals. We posit that such differences are likely due to differences in particle sizes [58] or covering with Si-poloxamers. FA/Si-CFEu particles are 140 nm compared to USPIO of 78 nm.

The presence of Si-CFEu nanoparticles in the reticuloendothelial tissues was confirmed by confocal microscopy and electron microscopy. Nanoparticles were co-localized with activated macrophages (Iba-1 staining) and elicited no adverse systemic responses in the animals as assessed by the serum chemistry profile and histological examination of vital organs. *In toto*, the current works have enabled the development of a screening dual-imaging nanoprobe for the non-invasive rapid assessment of drug nanoparticle biodistribution and screening of targeting moieties *in vivo*.

5. Conclusion

We have described the synthesis and characterization of FA/Si-CFEu nanoparticles “multimodal imaging nanoprobes” as sensitive and specific MRI contrast agents. The physicochemical properties of FA/Si-CFEu particles provide unique translational opportunities to enable real-time assessment of biodistribution of targeted nanoformulations and to nanoART. MRI evaluation of Si-CFEu in rats demonstrated robust T_2 signals in macrophage-rich regions of the reticuloendothelial system. Notably These data provide a first step towards assessing targeting moieties and provide a platform for incorporating drug into these constructs in order to develop theranostic particles for *in vivo* use.

Supplementary Material

Refer to Web version on PubMed Central for supplementary material.

Acknowledgments

The authors would like to thank Tom Bargar and Nicholas Conoan of the Electron Microscopy Core Facility (EMCF) at the UNMC for technical assistance. The EMCF is supported by state funds from the Nebraska Research Initiative (NRI) and the University of Nebraska Foundation, and institutionally by the Office of the Vice Chancellor for Research. The authors also would like to thank the UNMC Confocal Laser Scanning Microscopy and ICP-MS Core facilities and the Nebraska Center for Materials and Nanoscience at the University of Nebraska-Lincoln core facility for XRD, SQUID, AFM and HR-TEM. The authors would like to thank Melissa Mellon, Lirong Xu and Drs. Mariluz Arainga Ramirez, Prasanta Dash and Divya Prakash Gnanadhas for their thoughtful comments, active discussions and technical assistance. This work was supported in part by NIH Grant AG043540, DA028555, NS036126, NS034239, MH064570, NS043985, MH062261, AG043540 and DOD Grant 421-20-09A to HEG, the Carol Swarts Emerging Neuroscience Fund, a grant from the Nebraska Research Initiative (MB), and start-up funds from the Department of Pharmacology and Experimental Neuroscience

References

1. Vieira AC, Chaves LL, Pinheiro M, Ferreira D, Sarmento B, Reis S. Design and statistical modeling of mannose-decorated dapsone-containing nanoparticles as a strategy of targeting intestinal M-cells. Int J Nanomedicine. 2016; 11:2601–17. [PubMed: 27354792]
2. Shirasu T, Koyama H, Miura Y, Hoshina K, Kataoka K, Watanabe T. Nanoparticles Effectively Target Rapamycin Delivery to Sites of Experimental Aortic Aneurysm in Rats. PLoS One. 2016; 11(6):e0157813. [PubMed: 27336852]
3. Zhang M, Viennois E, Prasad M, Zhang Y, Wang L, Zhang Z, Han MK, Xiao B, Xu C, Srinivasan S, Merlin D. Edible ginger-derived nanoparticles: A novel therapeutic approach for the prevention and treatment of inflammatory bowel disease and colitis-associated cancer. Biomaterials. 2016; 101:321–40. [PubMed: 27318094]
4. Dash PK, Gendelman HE, Roy U, Balkundi S, Alnouti Y, Mosley RL, Gelbard HA, McMillan J, Gorantla S, Poluektova LY. Long-acting nanoformulated antiretroviral therapy elicits potent antiretroviral and neuroprotective responses in HIV-1-infected humanized mice. AIDS. 2012; 26(17):2135–44. [PubMed: 22824628]
5. Zhang G, Guo D, Dash PK, Arainga M, Wiederin JL, Haverland NA, Knibbe-Hollinger J, Martinez-Skinner A, Ciborowski P, Goodfellow VS, Wysocki TA, Wysocki BJ, Poluektova LY, Liu XM, McMillan JM, Gorantla S, Gelbard HA, Gendelman HE. The mixed lineage kinase-3 inhibitor URMC-099 improves therapeutic outcomes for long-acting antiretroviral therapy. Nanomedicine. 2016; 12(1):109–22. [PubMed: 26472049]
6. Puligujja P, Balkundi S, Kendrick L, Baldridge H, Hilaire J, Bade AN, Dash PK, Zhang G, Poluektova L, Gorantla S, Liu X-M, Ying T, Feng Y, Wang Y, Dimitrov DS, McMillan JM, Gendelman HE. Pharmacodynamics of long-acting folic acid-receptor targeted ritonavir boosted atazanavir nanoformulations. Biomaterials. 2015; 0:141–150.
7. Puligujja P, Arainga M, Dash P, Palandri D, Mosley RL, Gorantla S, Poluektova L, McMillan J, Gendelman HE. Pharmacodynamics of folic acid receptor targeted antiretroviral nanotherapy in HIV-1-infected humanized mice. Antiviral Res. 2015; 120:85–8. [PubMed: 26026666]
8. Arainga M, Guo D, Wiederin J, Ciborowski P, McMillan J, Gendelman HE. Opposing regulation of endolysosomal pathways by long-acting nanoformulated antiretroviral therapy and HIV-1 in human macrophages. Retrovirology. 2015; 12:5. [PubMed: 25608975]
9. Guo D, Li T, McMillan J, Sajja BR, Puligujja P, Boska MD, Gendelman HE, Liu X-M. Small magnetite antiretroviral therapeutic nanoparticle probes for MRI of drug biodistribution. Nanomedicine (London, England). 2014; 9(9):1341–1352.
10. Guo D, Zhang G, Wysocki TA, Wysocki BJ, Gelbard HA, Liu XM, McMillan JM, Gendelman HE. Endosomal trafficking of nanoformulated antiretroviral therapy facilitates drug particle carriage and HIV clearance. J Virol. 2014; 88(17):9504–13. [PubMed: 24920821]
11. Edagwa BJ, Zhou T, McMillan JM, Liu XM, Gendelman HE. Development of HIV reservoir targeted long acting nanoformulated antiretroviral therapies. Curr Med Chem. 2014; 21(36):4186–98. [PubMed: 25174930]
12. Puligujja P, McMillan J, Kendrick L, Li T, Balkundi S, Smith N, Veerubhotla RS, Edagwa BJ, Kabanov AV, Bronich T, Gendelman HE, Liu X-M. Macrophage Folate Receptor-Targeted Antiretroviral Therapy Facilitates Drug Entry Retention, Antiretroviral Activities Biodistribution for Reduction of Human Immunodeficiency Virus Infections. Nanomedicine: nanotechnology, biology, and medicine. 2013; 9(8)
13. Martinez-Skinner AL, Veerubhotla RS, Liu H, Xiong H, Yu F, McMillan JM, Gendelman HE. Functional proteome of macrophage carried nanoformulated antiretroviral therapy demonstrates enhanced particle carrying capacity. J Proteome Res. 2013; 12(5):2282–94. [PubMed: 23544708]
14. Gautam N, Roy U, Balkundi S, Puligujja P, Guo D, Smith N, Liu XM, Lamberty B, Morsey B, Fox HS, McMillan J, Gendelman HE, Alnouti Y. Preclinical pharmacokinetics and tissue distribution of long-acting nanoformulated antiretroviral therapy. Antimicrob Agents Chemother. 2013; 57(7): 3110–20. [PubMed: 23612193]
15. Roy U, McMillan J, Alnouti Y, Gautum N, Smith N, Balkundi S, Dash P, Gorantla S, Martinez-Skinner A, Meza J, Kanmogne G, Swindells S, Cohen SM, Mosley RL, Poluektova L, Gendelman HE. Pharmacodynamic and antiretroviral activities of combination nanoformulated antiretrovirals

in HIV-1-infected human peripheral blood lymphocyte-reconstituted mice. J Infect Dis. 2012; 206(10):1577–88. [PubMed: 22811299]

16. Klyachko NL, Haney MJ, Zhao Y, Manickam DS, Mahajan V, Suresh P, Hingtgen SD, Mosley RL, Gendelman HE, Kabanov AV, Batrakova EV. Macrophages offer a paradigm switch for CNS delivery of therapeutic proteins. Nanomedicine (Lond). 2014; 9(9):1403–22. [PubMed: 24237263]
17. Haney MJ, Zhao Y, Harrison EB, Mahajan V, Ahmed S, He Z, Suresh P, Hingtgen SD, Klyachko NL, Mosley RL, Gendelman HE, Kabanov AV, Batrakova EV. Specific transfection of inflamed brain by macrophages: a new therapeutic strategy for neurodegenerative diseases. PLoS One. 2013; 8(4):e61852. [PubMed: 23620794]
18. Zhao Y, Haney MJ, Mahajan V, Reiner BC, Dunaevsky A, Mosley RL, Kabanov AV, Gendelman HE, Batrakova EV. Active Targeted Macrophage-mediated Delivery of Catalase to Affected Brain Regions in Models of Parkinson's Disease. J Nanomed Nanotechnol. 2011:S4.
19. Kaminski R, Bella R, Yin C, Otte J, Ferrante P, Gendelman HE, Li H, Booze R, Gordon J, Hu W, Khalili K. Excision of HIV-1 DNA by gene editing: a proof-of-concept in vivo study. Gene Ther. 2016
20. Singh D, McMillan J, Hilaire J, Gautam N, Palandri D, Alnouti Y, Gendelman HE, Edagwa B. Development and characterization of a long-acting nanoformulated abacavir prodrug. Nanomedicine. 2016
21. Li T, Gendelman HE, Zhang G, Puligujja P, McMillan JM, Bronich TK, Edagwa B, Liu XM, Boska MD. Magnetic resonance imaging of folic acid-coated magnetite nanoparticles reflects tissue biodistribution of long-acting antiretroviral therapy. Int J Nanomedicine. 2015; 10:3779–90. [PubMed: 26082630]
22. Kumar A, Herbein G. The macrophage: a therapeutic target in HIV-1 infection. Mol Cell Ther. 2014; 2:10. [PubMed: 26056579]
23. Martinez-Picado J, Deeks SG. Persistent HIV-1 replication during antiretroviral therapy. Curr Opin HIV AIDS. 2016; 11(4):417–23. [PubMed: 27078619]
24. Datta PK, Kaminski R, Hu W, Pirrone V, Sullivan NT, Nonnemacher MR, Dampier W, Wigdahl B, Khalili K. HIV-1 Latency and Eradication: Past, Present and Future. Curr HIV Res. 2016
25. Wong JK, Yukl SA. Tissue reservoirs of HIV. Curr Opin HIV AIDS. 2016; 11(4):362–70. [PubMed: 27259045]
26. Fletcher CV, Staskus K, Wietgrefe SW, Rothenberger M, Reilly C, Chipman JG, Beilman GJ, Khoruts A, Thorkelson A, Schmidt TE, Anderson J, Perkey K, Stevenson M, Perelson AS, Douek DC, Haase AT, Schacker TW. Persistent HIV-1 replication is associated with lower antiretroviral drug concentrations in lymphatic tissues. Proc Natl Acad Sci U S A. 2014; 111(6):2307–12. [PubMed: 24469825]
27. Azhdarzadeh M, Atyabi F, Saei AA, Varnamkhasti BS, Omidi Y, Fateh M, Ghavami M, Shanehsazzadeh S, Dinarvand R. Theranostic MUC-1 aptamer targeted gold coated superparamagnetic iron oxide nanoparticles for magnetic resonance imaging and photothermal therapy of colon cancer. Colloids and Surfaces B: Biointerfaces. 2016; 143:224–232. [PubMed: 27015647]
28. Bhattacharya D, Behera B, Sahu SK, Ananthakrishnan R, Maiti TK, Pramanik P. Design of dual stimuli responsive polymer modified magnetic nanoparticles for targeted anti-cancer drug delivery and enhanced MR imaging. New Journal of Chemistry. 2016; 40(1):545–557.
29. Liang P-C, Chen Y-C, Chiang C-F, Mo L-R, Wei S-Y, Hsieh W-Y, Lin W-L. Doxorubicin-modified magnetic nanoparticles as a drug delivery system for magnetic resonance imaging-monitoring magnet-enhancing tumor chemotherapy. International Journal of Nanomedicine. 2016; 11:2021–2037. [PubMed: 27274233]
30. Mohapatra S, Rout SR, Das RK, Nayak S, Ghosh SK. Highly Hydrophilic Luminescent Magnetic Mesoporous Carbon Nanospheres for Controlled Release of Anticancer Drug and Multimodal Imaging. Langmuir. 2016; 32(6):1611–1620. [PubMed: 26794061]
31. Chan MH, Lin HM. Preparation identification of multifunctional mesoporous silica nanoparticles for in vitro in vivo dual-mode imaging theranostics and targeted tracking. Biomaterials. 2015; 46:149–58. [PubMed: 25678124]

32. Corr SA, Rakovich YP, Gun'ko YK. Multifunctional Magnetic-fluorescent Nanocomposites for Biomedical Applications. Nanoscale Research Letters. 2008; 3(3):87–104.
33. Thomas TP, Goonewardena SN, Majoros I, Kotlyar A, Cao Z, Leroueil PR, Baker JR. Folate-targeted nanoparticles show efficacy in the treatment of inflammatory arthritis. Arthritis and rheumatism. 2011; 63(9):2671–2680. [PubMed: 21618461]
34. Low PS, Henne WA, Doorneweerd DD. Discovery and Development of Folic-Acid-Based Receptor Targeting for Imaging and Therapy of Cancer and Inflammatory Diseases. Accounts of Chemical Research. 2008; 41(1):120–129. [PubMed: 17655275]
35. Gautam N, Puligujja P, Balkundi S, Thakare R, Liu X-M, Fox HS, McMillan J, Gendelman HE, Alnouti Y. Pharmacokinetics Biodistribution and Toxicity of Folic Acid-Coated Antiretroviral Nanoformulations. Antimicrobial Agents and Chemotherapy. 2014; 58(12):7510–7519. [PubMed: 25288084]
36. Guo D, Zhou T, Arainga M, Palandri D, Gautam N, Bronich T, Alnouti Y, McMillan J, Edagwa B, Gendelman HE. Creation of a Long-Acting Nanoformulated 2',3'-Dideoxy-3'-Thiacytidine. J Acquir Immune Defic Syndr. 2016
37. Gendelman HE, Orenstein JM, Martin MA, Ferrua C, Mitra R, Phipps T, Wahl LA, Lane HC, Fauci AS, Burke DS, et al. Efficient isolation and propagation of human immunodeficiency virus on recombinant colony-stimulating factor 1-treated monocytes. J Exp Med. 1988; 167(4):1428–41. [PubMed: 3258626]
38. Wu H, Liu G, Wang X, Zhang J, Chen Y, Shi J, Yang H, Hu H, Yang S. Solvothermal synthesis of cobalt ferrite nanoparticles loaded on multiwalled carbon nanotubes for magnetic resonance imaging and drug delivery. Acta Biomaterialia. 2011; 7(9):3496–3504. [PubMed: 21664499]
39. Allaedini G, Tasirin SM, Aminayi P. Magnetic properties of cobalt ferrite synthesized by hydrothermal method. International Nano Letters. 2015; 5(4):183–186.
40. Amiri S, Shokrollahi H. Magnetic structural properties of RE doped Co-ferrite (REåNd Eu and Gd) nano-particles synthesized by co-precipitation. Journal of Magnetism and Magnetic Materials. 2013; 345:18–23.
41. Naik SR, Salker AV. Change in the magnetostructural properties of rare earth doped cobalt ferrites relative to the magnetic anisotropy. Journal of Materials Chemistry. 2012; 22(6):2740–2750.
42. Mohamed RM, Rashad MM, Haraz FA, Sigmund W. Structure and magnetic properties of nanocrystalline cobalt ferrite powders synthesized using organic acid precursor method. Journal of Magnetism and Magnetic Materials. 2010; 322(14):2058–2064.
43. Sanpo N, Berndt CC, Wen C, Wang J. Transition metal-substituted cobalt ferrite nanoparticles for biomedical applications. Acta Biomaterialia. 2013; 9(3):5830–5837. [PubMed: 23137676]
44. Houshiar M, Zebhi F, Razi ZJ, Alidoust A, Askari Z. Synthesis of cobalt ferrite (CoFe2O4) nanoparticles using combustion coprecipitation, precipitation methods: A comparison study of size structuraland magnetic properties. Journal of Magnetism and Magnetic Materials. 2014; 371:43–48.
45. Mohapatra S, Rout SR, Maiti S, Maiti TK, Panda AB. Monodisperse mesoporous cobalt ferrite nanoparticles: synthesis and application in targeted delivery of antitumor drugs. Journal of Materials Chemistry. 2011; 21(25):9185–9193.
46. Lu L-Y, Yu L-N, Xu X-G, Jiang Y. Monodisperse magnetic metallic nanoparticles: synthesis performance enhancement and advanced applications. Rare Metals. 2013; 32(4):323–331.
47. Tahar LB, Artus M, Ammar S, Smiri LS, Herbst F, Vaulay MJ, Richard V, Grenèche JM, Villain F, Fiévet F. Magnetic properties of CoFe1.9RE0.1O4 nanoparticles (RE=La Ce Nd Sm Eu Gd, Tb Ho) prepared in polyol. Journal of Magnetism and Magnetic Materials. 2008; 320(23):3242–3250.
48. Lu LT, Dung NT, Tung LD, Thanh CT, Quy OK, Chuc NV, Maenosono S, Thanh NTK. Synthesis of magnetic cobalt ferrite nanoparticles with controlled morphology monodispersity, composition: the influence of solvent surfactant reductant and synthetic conditions. Nanoscale. 2015; 7(46): 19596–19610. [PubMed: 26542630]
49. Song Q, Zhang ZJ. Shape Control and Associated Magnetic Properties of Spinel Cobalt Ferrite Nanocrystals. Journal of the American Chemical Society. 2004; 126(19):6164–6168. [PubMed: 15137781]

50. Krejci AJ, Garcia A-M, Pham VH, Sun S, Dickerson JH. Comparing Highly Ordered Monolayers of Nanoparticles Fabricated Using Electrophoretic Deposition: Cobalt Ferrite Nanoparticles versus Iron Oxide Nanoparticles. Journal of The Electrochemical Society. 2015; 162(11):D3036–D3039.
51. Zhang Y, Lam YM. Controlled synthesis and association behavior of graft Pluronic in aqueous solutions. Journal of Colloid and Interface Science. 2007; 306(2):398–404. [PubMed: 17161416]
52. Su, Y-l, Wang, J., Liu, H-z. FTIR Spectroscopic Investigation of Effects of Temperature and Concentration on PEO-PPO-PEO Block Copolymer Properties in Aqueous Solutions. Macromolecules. 2002; 35(16):6426–6431.
53. Bowen CV, Zhang X, Saab G, Gareau PJ, Rutt BK. Application of the static dephasing regime theory to superparamagnetic iron-oxide loaded cells. Magnetic Resonance in Medicine. 2002; 48(1):52–61. [PubMed: 12111931]
54. Ruelas DS, Greene WC. An Integrated Overview of HIV-1 Latency. Cell. 2013; 155(3):519–529. [PubMed: 24243012]
55. Kimata JT, Rice AP, Wang J. Challenges and strategies for the eradication of the HIV reservoir. Curr Opin Immunol. 2016; 42:65–70. [PubMed: 27288651]
56. Joshi HM, Lin YP, Aslam M, Prasad PV, Schultz-Sikma EA, Edelman R, Meade T, Dravid VP. Effects of Shape and Size of Cobalt Ferrite Nanostructures on Their MRI Contrast and Thermal Activation. The Journal of Physical Chemistry C. 2009; 113(41):17761–17767.
57. Baldi G, Bonacchi D, Innocenti C, Lorenzi G, Sangregorio C. Cobalt ferrite nanoparticles: The control of the particle size and surface state and their effects on magnetic properties. Journal of Magnetism and Magnetic Materials. 2007; 311(1):10–16.
58. Zarschler K, Rocks L, Licciardello N, Boselli L, Polo E, Garcia KP, De Cola L, Stephan H, Dawson KA. Ultrasmall inorganic nanoparticles: State-of-the-art perspectives for biomedical applications Nanomedicine: Nanotechnology. Biology and Medicine. 2016; 12(6):1663–1701.
59. Yoon T-J, Yu KN, Kim E, Kim JS, Kim BG, Yun S-H, Sohn B-H, Cho M-H, Lee J-K, Park SB. Specific Targeting Cell Sortingand Bioimaging with Smart Magnetic Silica Core-Shell Nanomaterials. Small. 2006; 2(2):209–215. [PubMed: 17193022]
60. Marmorato P, Ceccone G, Gianoncelli A, Pascolo L, Ponti J, Rossi F, Salomé M, Kaulich B, Kiskinova M. Cellular distribution and degradation of cobalt ferrite nanoparticles in Balb/3T3 mouse fibroblasts. Toxicology Letters. 2011; 207(2):128–136. [PubMed: 21925252]
61. Kolosnjaj-Tabi J, Wilhelm C, Clément O, Gazeau F. Cell labeling with magnetic nanoparticles: Opportunity for magnetic cell imaging and cell manipulation. Journal of Nanobiotechnology. 2013; 11(1):1–19. [PubMed: 23343139]
62. Psimadas D, Baldi G, Ravagli C, Franchini MC, Locatelli E, Innocenti C, Sangregorio C, Loudos G. Comparison of the magnetic radiolabelinghyperthermic and biodistribution properties of hybrid nanoparticles bearing CoFe 2 O 4 and Fe 3 O 4 metal cores. Nanotechnology. 2014; 25(2):025101. [PubMed: 24334365]
63. Pillai V, Shah DO. Synthesis of high-coercivity cobalt ferrite particles using water-in-oil microemulsions. Journal of Magnetism and Magnetic Materials. 1996; 163(1–2):243–248.
64. Kim T, Momin E, Choi J, Yuan K, Zaidi H, Kim J, Park M, Lee N, McMahon MT, Quinones-Hinojosa A, Bulte JWM, Hyeon T, Gilad AA. Mesoporous Silica-Coated Hollow Manganese Oxide Nanoparticles as Positive T1 Contrast Agents for Labeling and MRI Tracking of Adipose-Derived Mesenchymal Stem Cells. Journal of the American Chemical Society. 2011; 133(9):2955–2961. [PubMed: 21314118]
65. Lu Y, Yin Y, Mayers BT, Xia Y. Modifying the Surface Properties of Superparamagnetic Iron Oxide Nanoparticles through A Sol-Gel Approach. Nano Letters. 2002; 2(3):183–186.
66. Kim J, Kim HS, Lee N, Kim T, Kim H, Yu T, Song IC, Moon WK, Hyeon T. Multifunctional Uniform Nanoparticles Composed of a Magnetite Nanocrystal Core and a Mesoporous Silica Shell for Magnetic Resonance and Fluorescence Imaging and for Drug Delivery. Angewandte Chemie International Edition. 2008; 47(44):8438–8441. [PubMed: 18726979]
67. Ming Z, Brian LC, Charles JOC. Synthesis and characterization of monodisperse ultra-thin silica-coated magnetic nanoparticles. Nanotechnology. 2008; 19(8):085601. [PubMed: 21730725]

68. Yoon T-J, Kim JS, Kim BG, Yu KN, Cho M-H, Lee J-K. Multifunctional Nanoparticles Possessing A “Magnetic Motor Effect” for Drug or Gene Delivery. Angewandte Chemie. 2005; 117(7):1092–1095.

69. Chen F-H, Zhang L-M, Chen Q-T, Zhang Y, Zhang Z-J. Synthesis of a novel magnetic drug delivery system composed of doxorubicin-conjugated Fe3O4 nanoparticle cores and a PEG-functionalized porous silica shell. Chemical Communications. 2010; 46(45):8633–8635. [PubMed: 20941412]

Statement of Significance

A novel europium (Eu^{3+}) doped cobalt ferrite (Si-CFEu) nanoparticle was produced for use as an bioimaging probe. Its notable multifunctional, fluorescence and imaging properties, allows its use for rapid screenings of future drug biodistribution tests. Decoration of the Si-CFEu particles with folic acid showed by greater than a log order-of-magnitude in sensitivity and specificity for magnetic resonance imaging over a more conventional ultrasmall superparamagnetic iron oxide particle, when both particles were administered at equivalent iron doses. The potential use of these particles in theranostic tests will serve as a platform for designing improved drug delivery strategies to combat inflammatory and infectious diseases.

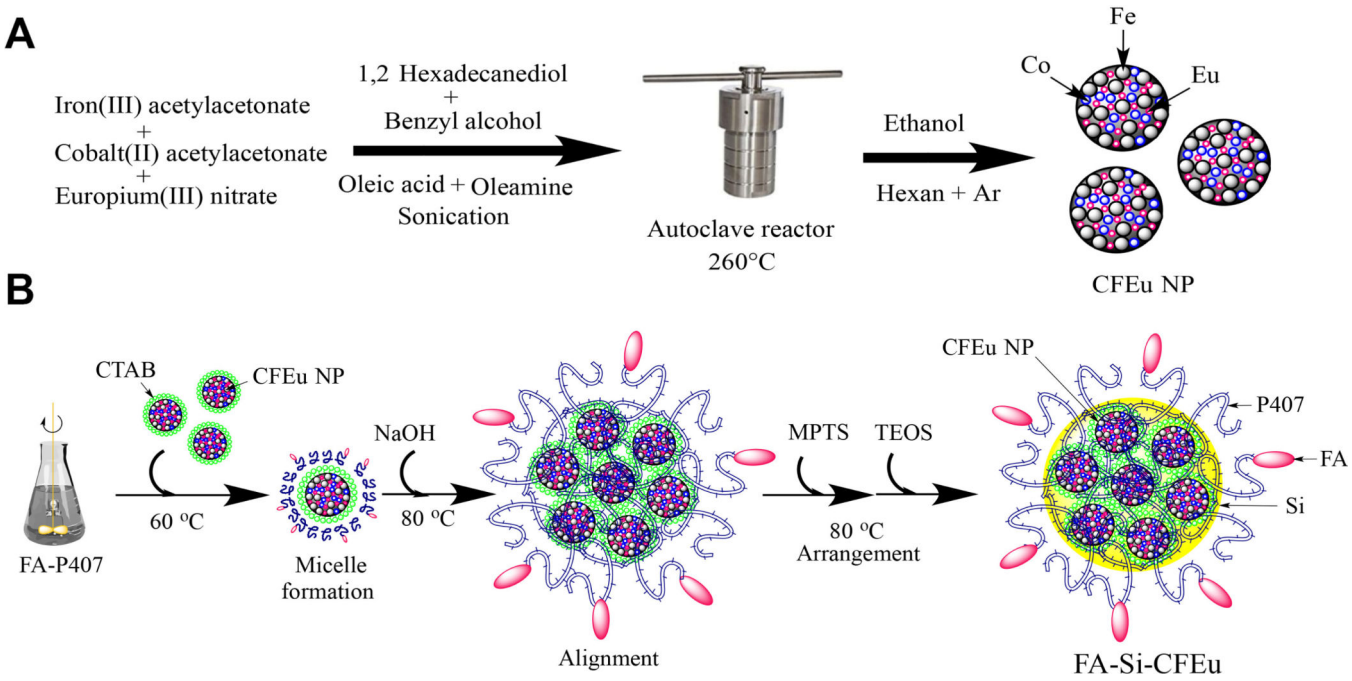

Fig. 1. Synthesis of CFEu and FA-Si-CFEu NP

The nanoparticle synthesis is illustrated in panels A and B. (A) Step-wise scheme for the synthesis of CFEu nanoparticles (Iron, coblt and europium). The particles were manufactured by a modified solvothermal technique. (Graphical descriptions of colors; Black spheres= iron; blue spheres = cobalt and red spheres = europium) (B) The steps required for entrapment of Eu^{3+} doped CFEu nanoparticles into core-shell Si-P407, and for decoration of Si-CFEu with FA to improve the active targeting of monocyte-macrophages are shown (Graphical descriptions of colors; Pink beads = folic acid, FA; Yellow = silica matrix, and blue = poloxamer 407).

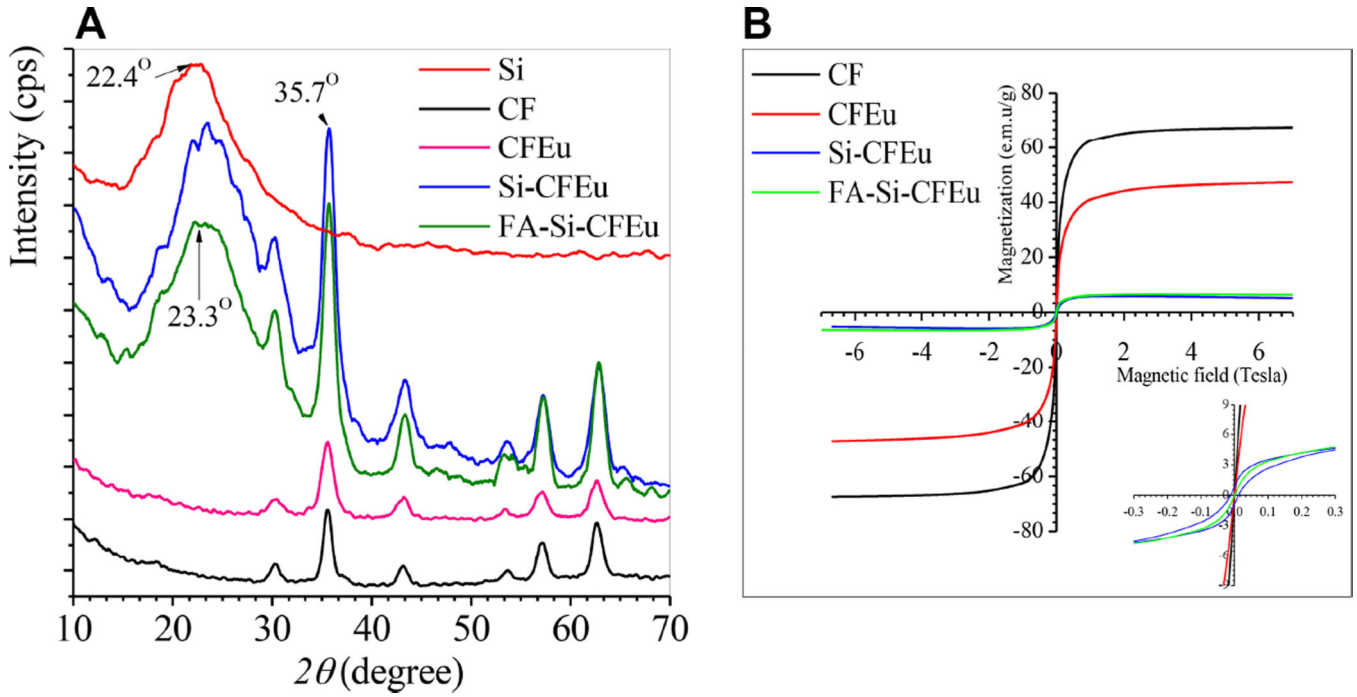

Fig. 2. Structural and magnetic properties characterizations

The structural and magnetic properties of the synthesized CF, CFEu and FA/Si-CFEu nanoparticles is illustrated in A and B. (A) X-ray powder diffraction (XRD) patterns, and (B) Magnetic-Hysteresis (M-H) curve measurements are shown employing a SQUID magnetometer. Data are recorded at T = 300 K.

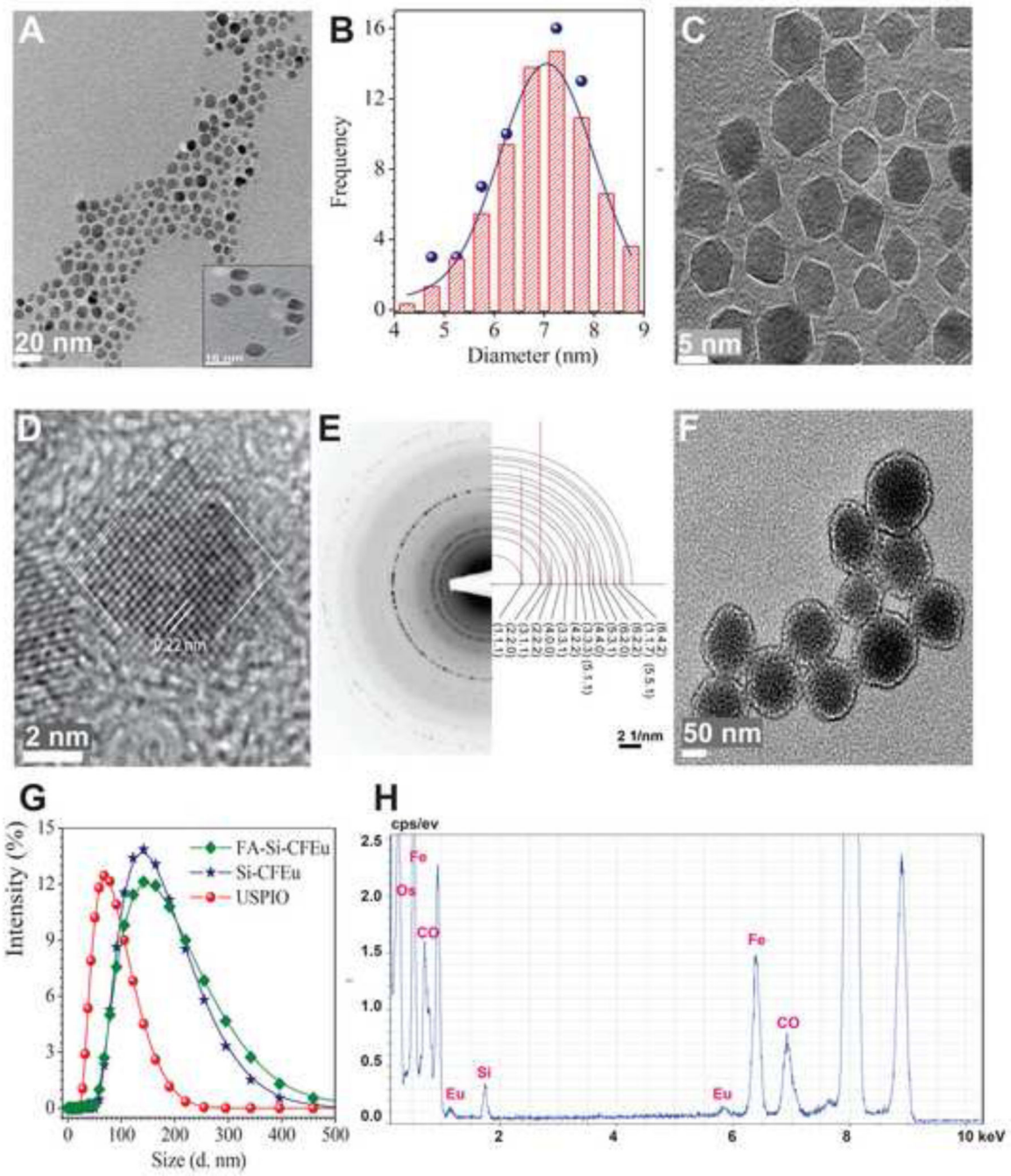

Fig. 3. Morphology and physical-chemical profiles of the CFEu and Si-CFEu nanoparticles

(A-G) High-resolution transmission electron microscopy (TEM) images of CFEu nanoparticles. (A) The distribution pattern of the particles is shown in a lower field image, scale = 20 nm with the insets demonstrating a ring pattern arrangement, scale = 10 nm. (B) A histogram illustrates the nanoparticles size distribution and an average size of the particles was 7.2 nm. (C) In a high resolution image, the facetted shape and dimensions of the particles are shown, scale = 5 nm. (D) A complete structural morphological pattern of particle is shown with lattice fringes, scale = 2 nm. (E) Electron diffraction pattern of CFEu

nanoparticles is shown. Simulation indexation (PCED2s) of the observed lines corresponds to the characteristic interplanar spacings of the crystal structure. (F) Si-CFEu nanoparticles with uniform Si-P407 shells coverd on CFEu nanoparticles, scale = 50 nm. (G) Hydrodynamic size distribution of USPIO, Si-CFEu and FA-Si-CFEu nanoparticles by dynamic light scattering (DLS). (H) Distribution of metals is measured with energy dispersive x-ray spectroscopy.

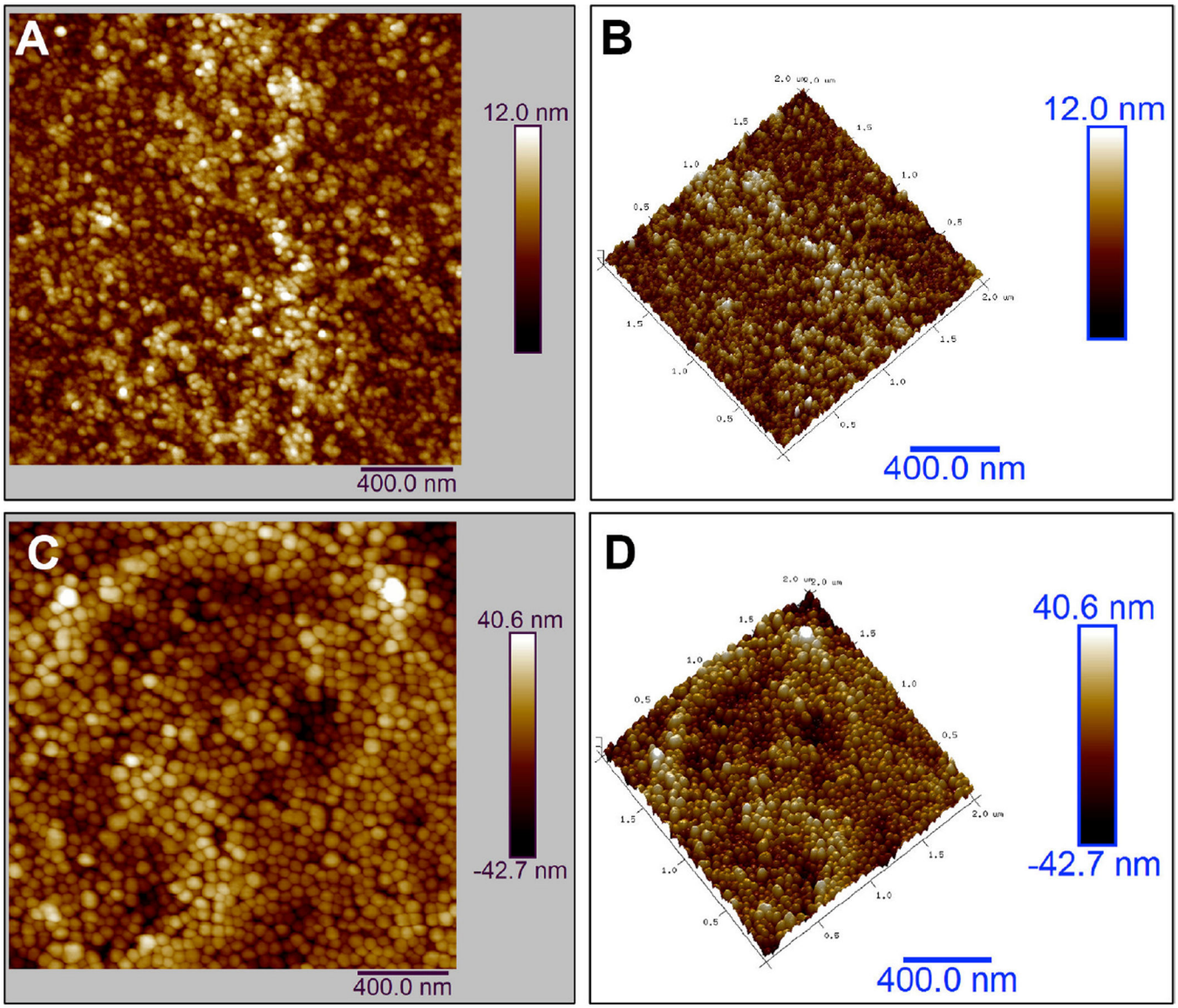

Fig. 4. Characterization of the distribution of CFEu and Si-CFEu nanoparticles by AFM

AFM topography of (A) distribution of CFEu nanoparticles and (B) a corresponding 3D view are shown. AFM topography of (C) Si-CFEu nanoparticles with (D) a corresonding 3D view are illustrated.

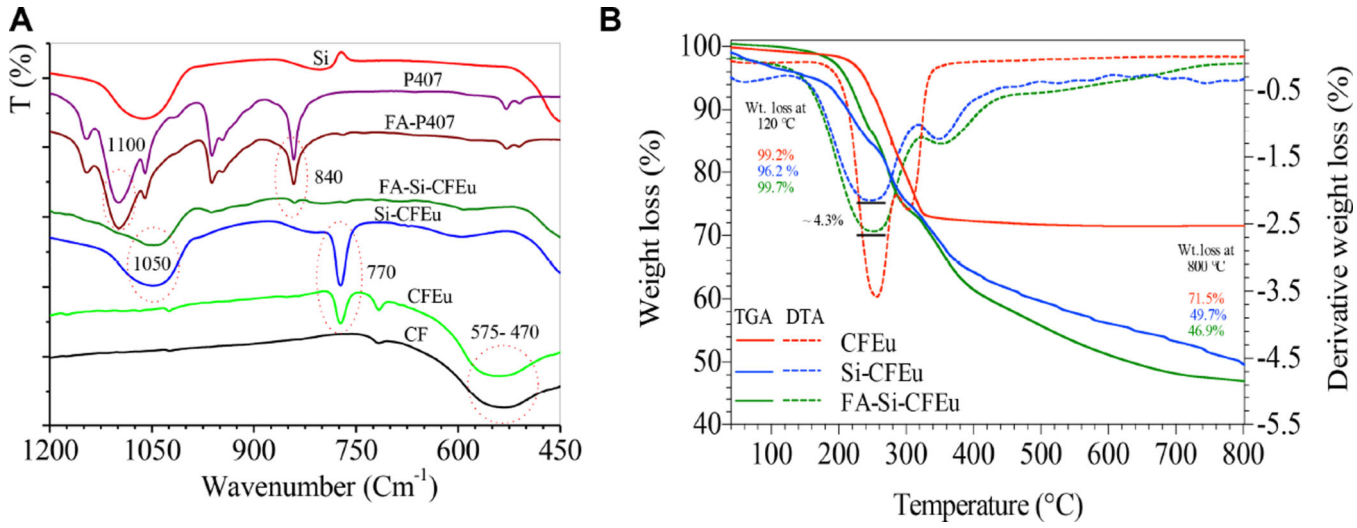

Fig. 5. FTIR and thermal properties of nanoparticles

(A) FTIR spectra and (B) thermal gravimetric (TGA) and differential thermal analysis (DTA) analysis of the CFEu nanoparticles and FA/Si-CFEu nanoparticles. (Fig. 5. panel B: Solid lines are TGA data and dotted lines are DTA data Where: Red line shown= CFEu, blue line shown = Si-CFEu and green line shown= FA-Si-CFEu).

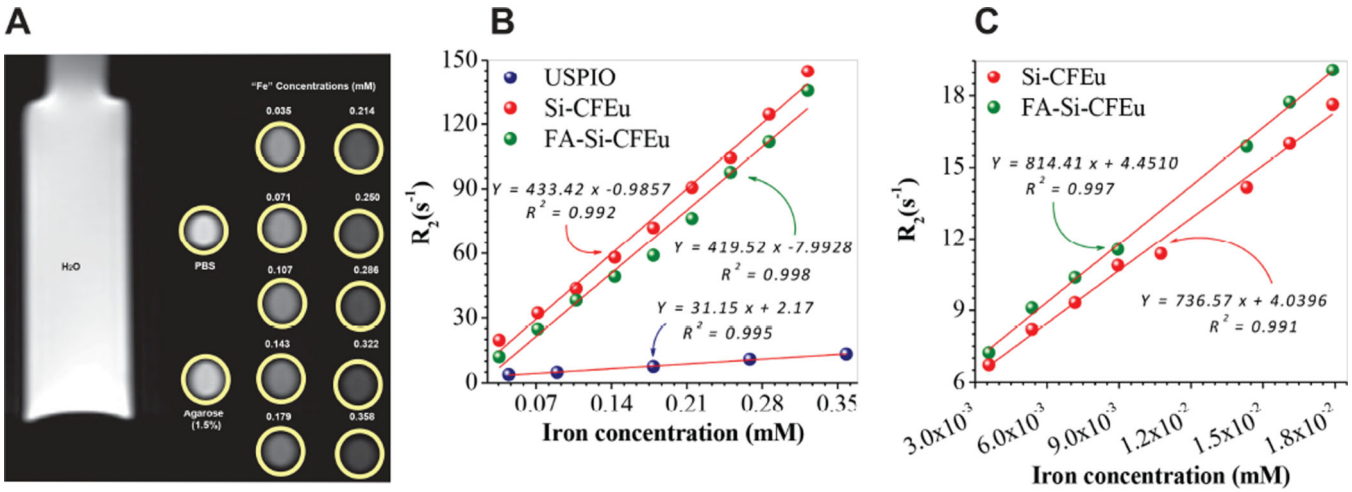

Fig. 6. Macrophage uptake, retention and particle distribution

FA-Si-CFEu and Si-CFEu were added to human MDM culture medium at 150 ng/mL iron concentration. (A) Time course of MDM uptake of nanoparticles over 8 hours. (B) MDM retention of nanoparticles was determined over 10 days following an 8 hour nanoparticle loading. For MDM uptake and retention, cell lysates at indicated time points were analysed by inductively coupled plasma mass spectrometry (ICP-MS) for cobalt ion concentrations. Data are expressed as mean ± SEM, n = 3 (*:$p<0.05$). (C) Intracellular nanoparticles were detected by confocal microscopy at an excitation 488 nm and emission of 510/520 nm. Images were captured with 63× objective. (D) Typical internal morphology of MDM cell in transmission electron microscopy (TEM) is shown in control cell image and detail morphology at area of interest were presented in corresponding magnified images (ii-iii), (E-F) Intracellular uptake of Si-CFEu and FA-Si-CFEu nanoparticles by TEM images with nanoparticles location areas were presented in corresponding magnified images (ii-iii), (E) The Si-CFEu nanoparticles internalized and entrapped in endosomes vessicles of macrophages (F) FA-Si-CFEu nanoparticles treated macrophages images demonstrated higher number of particles internalized in vesicles as compared to Si-CFEu. Details of the internalization and entrapment of the nanoparticles are made in this illustration. Vesicles containing nanoparticles (dark) are visibly in zoom images of red dotted line circles in the macrophage.

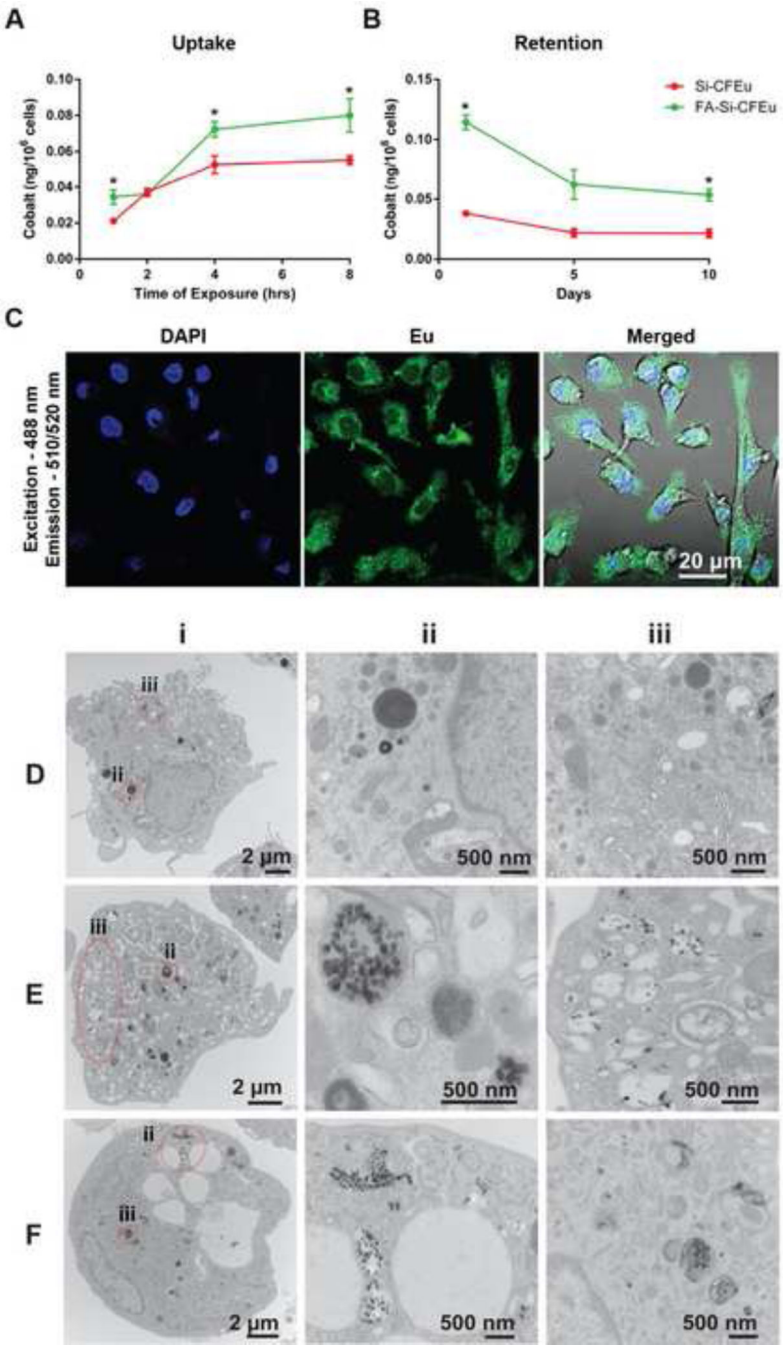

Fig. 7. *In vitro* relaxivity measurements

(A) T_2 weighted MRI phantom images of Si-CFEu nanoparticles at various concentrations of iron. (B) The r_2 relaxivity rates comparison between the FA/Si-CFEu and USPIO nanoparticles suspensions in PBS and (C) The r_2 relaxivity rates comparison between Si-CFEu and FA-Si-CFEu nanoparticles loaded MDM. r_2 relaxivity of nanoparticles with agarose gel samples containing varied concentrations of iron was measured.

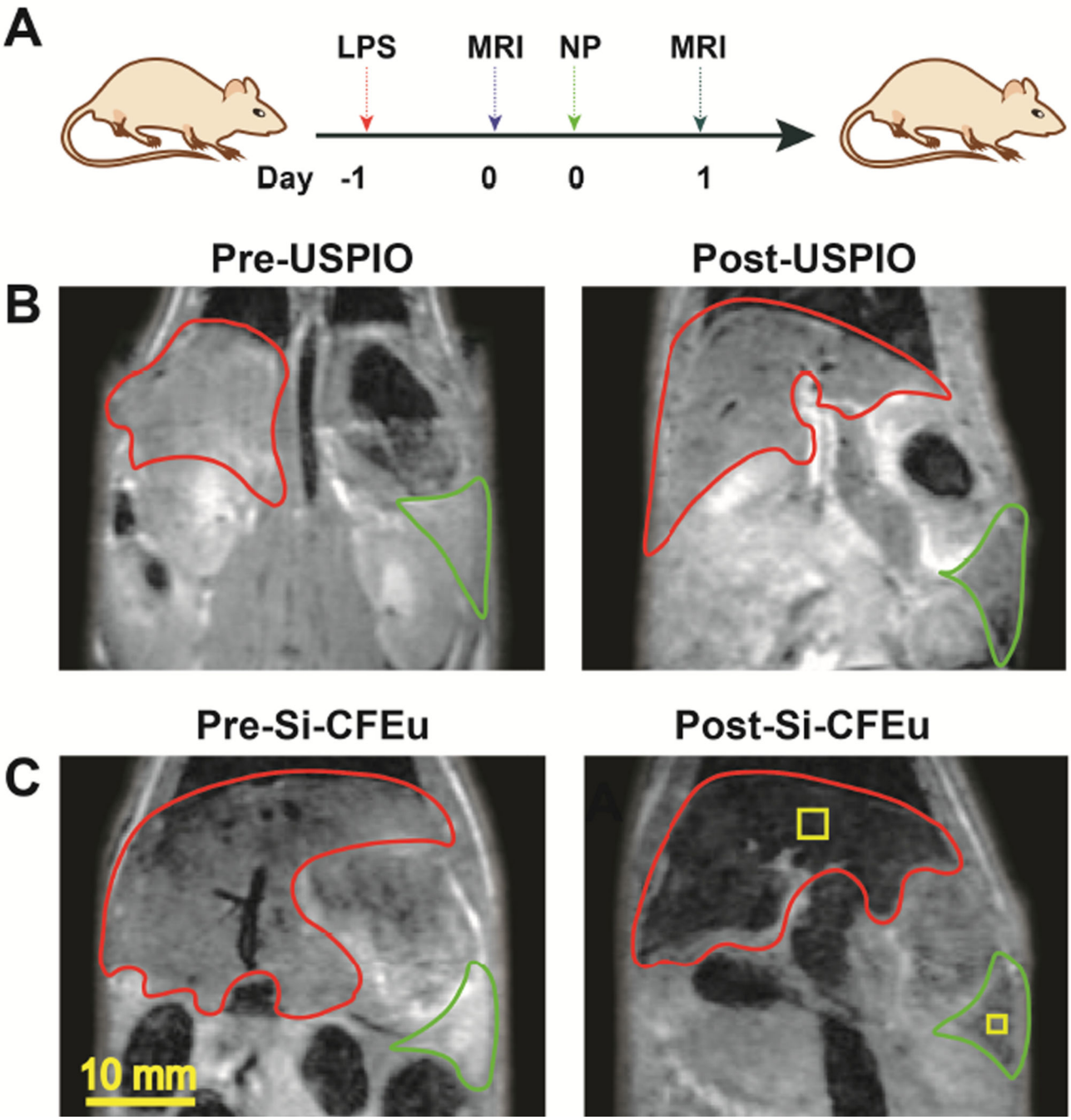

Fig. 8. Assessments of Si-CFEu and USPIO nanoparticle biodistribution by MRI tests

(A) The time line of the experimental procedure is shown (LPS: Lipopolysaccharide, 5 mg/kg; MRI: magnetic resonance imaging scaning: NP: Nanoparticles). The representative T_2 maps of magnetic resonance (MR) images of rats (B) with pre-(left) and 24 hours after (right) 1 mg iron/kg IV administration of USPIO nanoparticle and (C) Si-CFEu nanoparticles, respectively (red: liver and green:spleen).

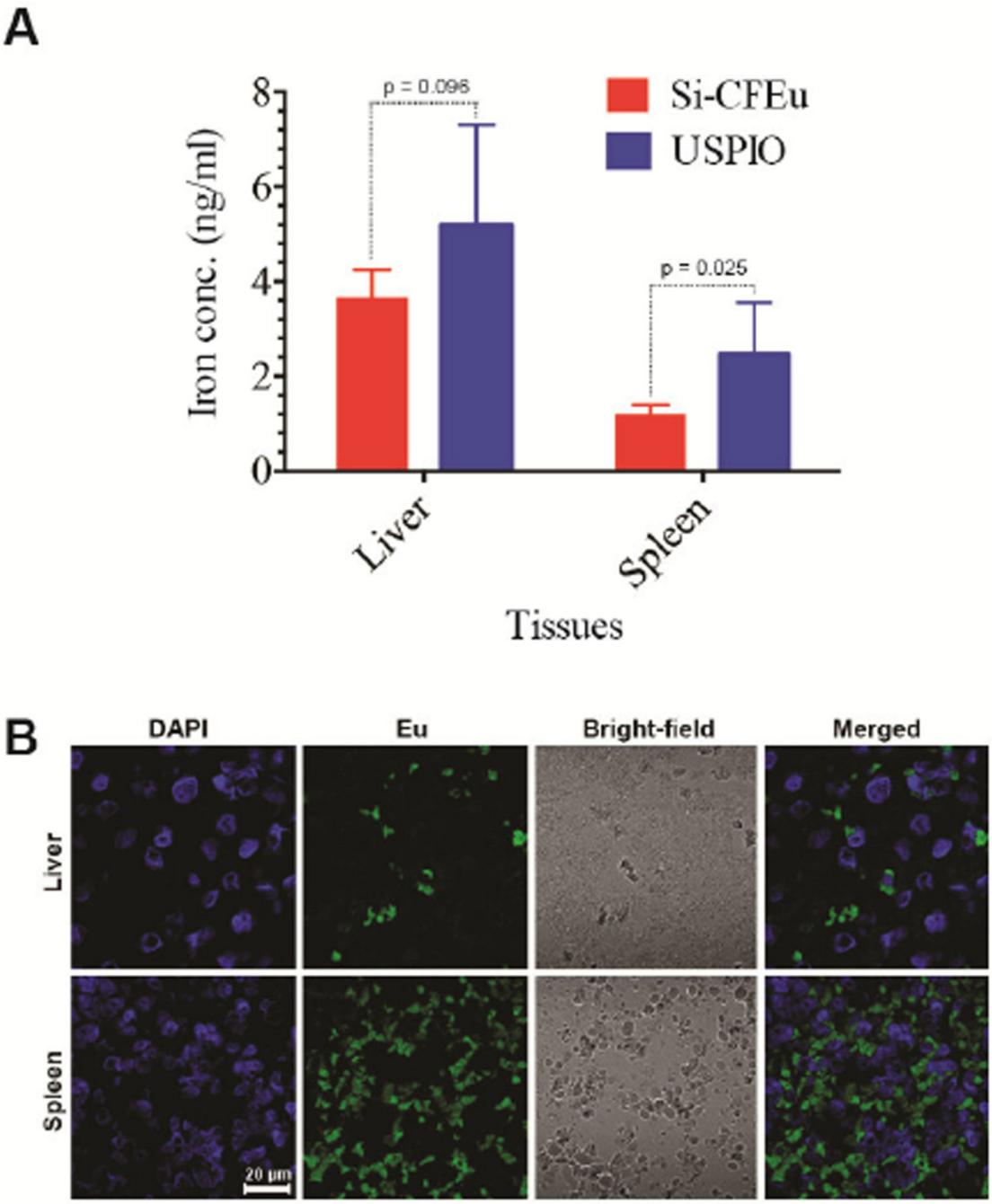

Fig. 9. T_2 image and histology correlations with quantitatively measurements of biodistributions

(A) Comparison of iron concentration quantitatively measurement of Si-CFEu and USPIO nanoparticles in liver and spleen, 24 hours after 1 mg iron /kg IV administration. (B) Si-CFEu nanoparticles biodistribution with MRI T_2 mapping and immunohistology correlations in the regions of interest. The liver and spleen MRI T_2 maps from Si-CFEu nanoparticles treated rats. The yellow squares in Fig.8 C. Right panel are indicate typical areas of interest corresponding to tissues, where the T_2 would be measured in order to estimate Si-CFEu nanoparticles concentration.

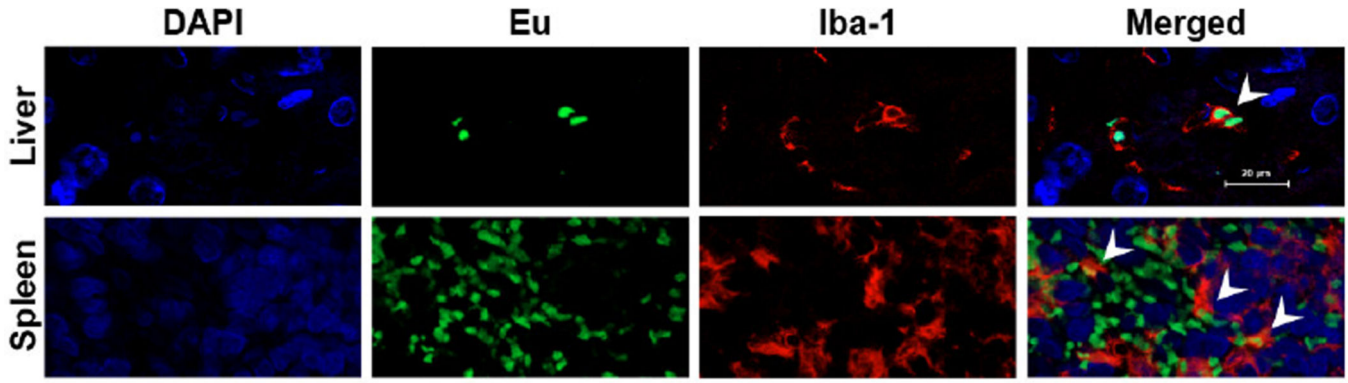

Fig. 10. Monocyte-macrophage Si-CFEu nanoparticle uptake

Representative tissue sections of liver and spleen of rats administered with Si-CFEu nanoparticles (green) and stained for Iba-1 (red) on activated macrophages are presented. Nanoparticles were detected in both liver and spleen. Co-localization of nanoparticles within macrophages is indicated by arrows (orange) in the merged figures. Images were captured with 63X objective.

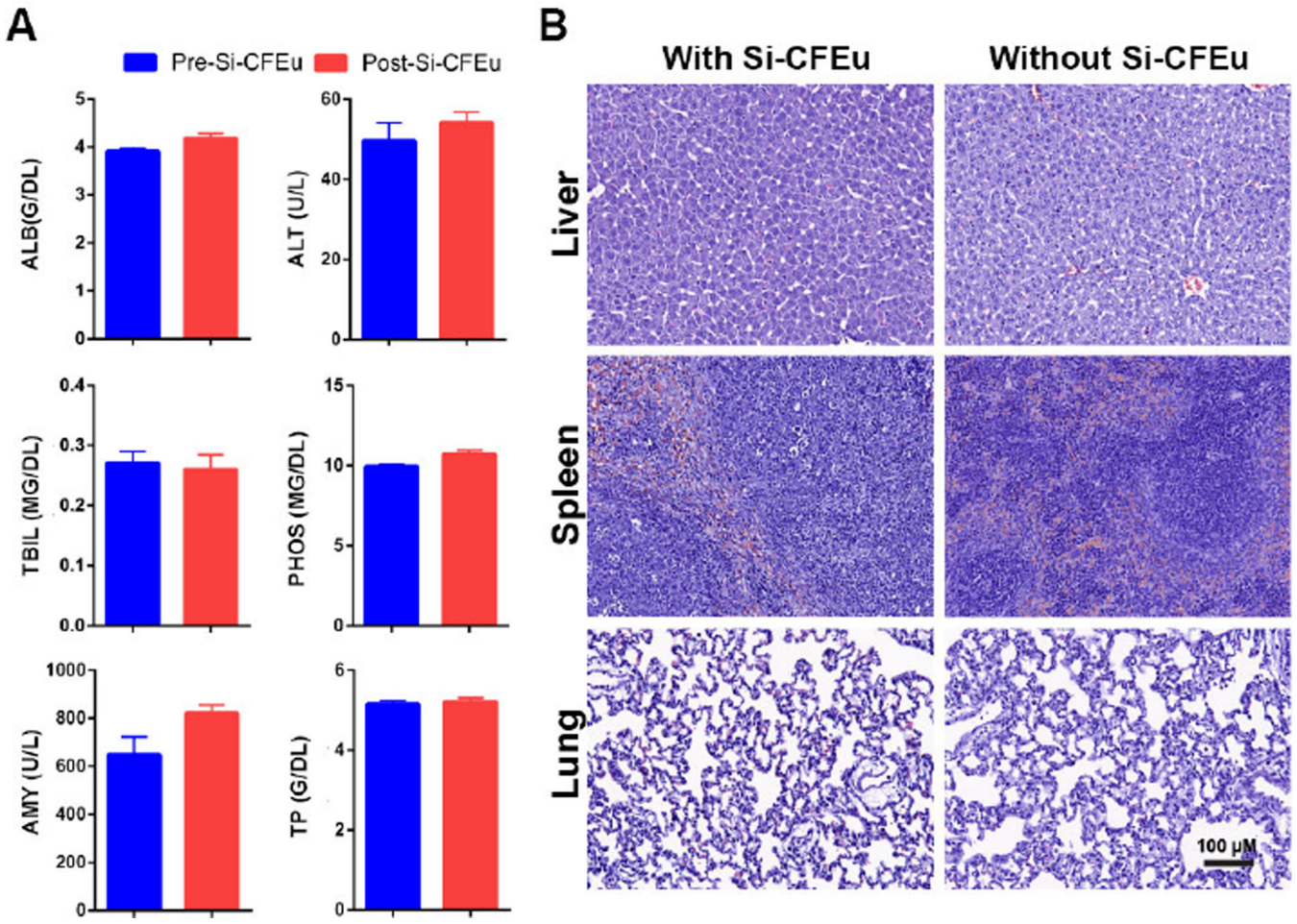

Fig. 11. Toxicity tests after Si-CFEu nanoparticle administration

(A) Hepatic, renal and pancreatic functions (serum chemistry profile) were analyzed in rats pre-and post-Si-CFEu nanoparticles administration (ALB:Albumin, ALT: Alanine aminotransferase, TBIL: Total bilirubin, AMY: Amylase, PHOS: Phosphate, TP: Total protein). (B) H&E staining of liver, spleen and lungs of rats with and without administration of Si-CFEu nanoparticles. No abnormal pathology was detected in tissues in either group. Images were captured with 20× objective. (Pre-nanoparticle administration: 24 hours after 5 mg/kg LPS and prior to Si-CFEu nanoparticle administration).